Structural organization of p62 filaments and the cellular ultrastructure of calcium-rich p62-enwrapped lipid droplet cargo

Author information

Sabrina Berkamp[1#], Lisa jungbluth[1#], Alexandros Katranidis[1#], Siavash Mostafavi[1], Olivera Korculanin[1,5], Peng-Han Lu[2], Lokesh Sharma[3], Lipi Thukral[3,4], Jörg Fitter[1,5], Rafal E. Dunin-Borkowski[2], Carsten Sachse[1,6†]

[1]Ernst-Ruska Centre for Microscopy and Spectroscopy with Electrons, ER-C-3/Structural Biology, Forschungszentrum Jülich, 52425 Jülich, Germany.

[2]Ernst-Ruska Centre for Microscopy and Spectroscopy with Electrons, ER-C-1/Physics of Nanoscale Systems, Forschungszentrum Jülich, 52425 Jülich, Germany

[3]Computational Structural Biology Lab, CSIR-Institute of Genomics and Integrative Biology, Mathura Road, New Delhi 110025, India

[4]Academy of Scientific and Innovative Research (AcSIR), Ghaziabad 201002, India

[5]RWTH Aachen, I.Physikalisches Institut (IA), Aachen, Germany

[6]Department of Biology, Heinrich Heine University, Universitätsstr. 1, 40225 Düsseldorf, Germany.

[#]These authors contributed equally

[†] Correspondence: c.sachse@fz-juelich.de (C.S.)

Keywords: cryo-electron microscopy, helical reconstruction, autophagy, p62/SQSTM1, liquid-liquid phase separation, cryo-electron tomography, correlative light and electron microscopy (CLEM), focused ion beam scanning electron microscopy (FIB-SEM), energy-dispersive X-ray (EDX) spectroscopy, lipid droplets, lipophagy

Abstract

The selective autophagy receptor p62/SQSTM1 (from hereon p62) is known to form higher-order filaments in vitro and to undergo liquid-liquid phase separation when mixed with poly-ubiquitin. We determined the full-length cryo-EM structure of p62 and elucidated a structured double helical filament scaffold composed of the PB1-domain associated with the flexible C-terminal part residing in the lumen and the solvent-accessible major groove. At different pH values and upon binding to soluble LC3, LC3-conjugated membranes and poly-ubiquitin, we observed p62 filament re-arrangements in the form of structural unwinding, disassembly, lateral association and bundling, respectively. In the cellular environment, under conditions of ATG5 knockdown leading to stalled autophagy, we imaged high-contrast layers consisting of p62 oligomers enwrapping lipid droplets by cryogenic electron tomography in cellulo, which we identified as calcium phosphate by compositional spectroscopy analysis. Together, we visualized the cellular ultrastructure of p62 oligomers with high calcium content as a potential intermediate step of autophagy initiation.

43 # Introduction

44 Autophagy is a conserved cellular process that degrades and recycles cytoplasmic
45 material such as aggregated proteins, damaged organelles and pathogens to
46 maintain intracellular homeostasis (Mizushima et al., 2011; Wen & Klionsky, 2016).
47 While autophagy operates at a basal level for routine maintenance, it can also be
48 activated by stress factors like nutrient deprivation, hypoxia and DNA damage
49 (Kroemer et al., 2010). There are three main autophagy pathways: macroautophagy,
50 microautophagy and chaperone-mediated autophagy. In macroautophagy (from here
51 on simply referred to as autophagy), an autophagosome forms within the cytoplasm
52 to enclose cellular material that is subsequently degraded and recycled after fusing
53 with a lysosome. A series of defined autophagy core machinery complexes mediate
54 the progression of cellular autophagy: Atg1/ULK1 kinase, PI-3 kinase, ATG9 lipid
55 scramblase, the ATG2-ATG18 lipid transfer complex and two ubiquitin-like
56 conjugation systems (Xie & Klionsky, 2007). The recognition of cargo can proceed in
57 a non-selective or in a selective manner by either enclosing the bulk stochastically or
58 through specific binding by selective autophagy receptors, respectively (Y. Feng et
59 al., 2014).

60 Selective autophagy requires cargo receptors that recognize poly-ubiquitinated cargo
61 and interact with Atg8 family proteins (Kraft et al., 2014; Y.-K. Lee & Lee, 2016). The
62 Atg8 family contains ubiquitin-like proteins: Atg8 in yeast and microtubule-associated
63 protein 1 light chain 3 (LC3) as well as gamma-aminobutyric acid type A receptor-
64 associated protein (GABARAP) in mammals (Shpilka et al., 2011). The conjugation
65 of Atg8 proteins to the lipid membrane is essential for phagophore membrane
66 expansion (Mizushima et al., 2001) and is mediated by two autophagy-specific
67 ubiquitin-like conjugation systems: ATG12-ATG5 and the LC3 conjugation system
68 (Nakatogawa et al., 2009). Selective autophagy receptors, like p62/SQSTM1 (from
69 here on: p62) (Bjørkøy et al., 2005), contain an LC3-interacting region (LIR) motif
70 that facilitates interaction with Atg8 proteins and a ubiquitin-binding domain
71 (Birgisdottir et al., 2013; Rogov et al., 2014). In the meantime, a series of additional
72 autophagy receptors have been identified with LIR motifs as well as ubiquitin binding
73 abilities in order to confer specificity and redundancy in the cargo recognition and
74 removal. For instance, for mitophagy NBR1, optineurin, NDP52 and TAXBP1 have
75 been characterized in addition to p62 (Lazarou et al., 2015). While p62 knock-outs
76 are viable for an organism, long-term benefits of increased p62 levels have been
77 found to promote proteastasis and longevity in response to stress in C.*elegans*
78 (Kumsta et al., 2019).

79 p62 has a key role in selective autophagy by recognizing poly-ubiquitinated cargo
80 and delivering it to the autophagosome (Bjørkøy et al., 2005). Originally, p62 was
81 described as an interaction partner for tyrosine-protein kinase Lck (Joung et al.,
82 1996), while it was also shown to be involved in multiple pathways including Wnt,
83 Nrf2, mTORC and NF-κB signaling (Puissant et al., 2012). In the NF-κB pathway,
84 p62 can interact with MEKK3, MEK5, aPKCs (Lamark et al., 2003) and tumor
85 necrosis factor receptor associated factor 6 (TRAF6) as a mediator in tumorigenesis
86 (Duran et al., 2011). Moreover, p62 actively promotes the spatio-temporal
87 organization of autophagy downstream effectors such as FIP200 at the cargo site
88 (Turco et al., 2019). p62 is a multi-domain protein with a Phox1 and Bem1p (PB1)
89 domain, followed by a ZZ-domain and an intrinsically disordered region (IDR) up to
90 the C-terminal ubiquitin-binding associated (UBA) domain. The PB1 domain is
91 responsible for p62 polymerization into long flexible filaments (Ciuffa et al., 2015;
92 Jakobi et al., 2020) and was shown to be critical for its function in autophagy as
93 polymerization deficient mutations excluded p62 from the autophagosome formation
94 site (Itakura & Mizushima, 2011). The IDR contains several relevant interaction
95 motifs, including the LIR and KEAP1-interacting region (KIR) motif (Komatsu et al.,
96 2010). The C-terminal UBA domain captures poly-ubiquitinated cargo (Ciani et al.,
97 2003). The autophagy receptor NBR1 is structurally the most similar to p62 amongst
98 the autophagy receptors as it is closely evolutionarily related and directly interacts
99 with p62 via its PB1 domain albeit it is unable to form higher-order oligomers or
100 filaments (Jakobi et al., 2020; Kirkin et al., 2009).

101 p62 is a well-studied cargo receptor that recognizes and removes various different
102 cellular cargoes: aggregated proteins in aggrephagy (Bjørkøy et al., 2005; Pankiv et
103 al., 2007), damaged peroxisomes in pexophagy (Zhang et al., 2015) and lipid
104 droplets in lipophagy (L. Wang et al., 2017; Yan et al., 2019). For lipophagy, the size
105 of the removed lipid droplets is smaller than one μm while larger lipid droplets were
106 shown to be predominantly degraded by lipolysis (Schott et al., 2019). At the same
107 time, lipid droplets are a special cargo in the context of autophagy as they can also
108 serve as a direct or indirect lipid source for the growing phagophore mediated by
109 direct contact in addition to the ATG9A vesicles or ATG2 lipid bridges (Dupont et al.,
110 2014; Korfhage et al., 2023; Mailler et al., 2021; Shpilka et al., 2015). Lipid droplets
111 were also found to serve as direct substrates for non-canonical autophagy during
112 prolonged starvation after LC3-conjugation (Omrane et al., 2023).

113 p62 has also been shown to undergo liquid-liquid phase separation (Brangwynne et
114 al., 2009) induced by poly-ubiquitin interaction with multiple polymerized p62 entities

115 in vitro (Sun et al., 2018; Zaffagnini et al., 2018a). However, in vivo, p62 phase
116 separated condensates recruit many autophagy regulators that can affect the
117 mobility of the separated phase and as a result autophagy efficiency. For instance,
118 Keap1 over-expression was observed to increase the rigidity of p62 condensates,
119 thus promoting autophagy (Y. Lee et al., 2017). NBR1 enhances p62 condensate
120 formation and poly-ubiquitin affinity (Turco et al., 2021). In addition to binding
121 partners, the oligomeric state of p62 and post-translational modifications can affect
122 the phase separation properties, e.g., as the IDR of p62 harbors the KIR motif that
123 when post-translationally modified has been shown to enhance the interaction with
124 Keap1 (Ichimura et al., 2013). The quaternary structural organization of p62 presents
125 another level of regulation for cellular phase separation as phosphorylation of the
126 PB1 domain by PKA was identified and shown to disrupt PB1 domain interactions
127 (Christian et al., 2014).

128 In order to improve our detailed structural understanding of purified p62, we
129 determined the cryo-electron microscopy (cryo-EM) structure of full-length p62. The
130 structure revealed the double helical organization of an N-terminal PB1-domain
131 scaffold while the more poorly resolved partially disordered C-terminal part resided in
132 the lumen and the major groove of the assembly. Binding studies of LC3b and poly-
133 ubiquitin showed that p62 filaments can undergo structural re-arrangements of
134 disassembly or filament bundling, respectively. When p62 filaments were added to
135 LC3b-conjugated membranes, they associate laterally and also unwind their regular
136 helical structures into bubbles at physiological pH. Native ultrastructural imaging of
137 p62-positive structures using cryo-electron tomography (cryo-ET) in ATG5 depleted
138 RPE1 cells revealed stalled intermediate autophagy stages of p62-enwrapped lipid
139 droplets. Interestingly, the surrounding p62 layer had a dark contrast and contained
140 high levels of calcium and phosphorus based on energy-dispersive X-ray
141 spectroscopy analysis (EDX). The high-resolution visualization of p62-enwrapped
142 cargo together with calcium may present an important intermediate state of
143 autophagy initiation.

144 Results

145 p62 forms a double-helical filament with a PB1 scaffold and a flexible C-
146 terminus in the major groove

147 Previously, we determined the three-dimensional (3D) cryo-EM structure of the p62-
148 PB1 domain arranged in a series of different filamentous assemblies (Jakobi et al.,
149 2020). In order to advance our structural understanding of full-length human p62, we

150 optimized the previous preparations of full-length p62 for improved homogeneity. As
151 previous studies suggested an effect of pH on the assembly conditions (Kwon et al.,
152 2018), we compared the preparations at different pHs. Classifications of small cryo-
153 EM test data sets revealed that at pH=6 the majority of the filament classes were
154 helically regular while at pH=8 a large fraction of them were found unwound
155 resembling an open bubble (**Supplementary Fig. 1A**). Therefore, we recorded a full
156 cryo-EM data set at pH=6 revealing long and flexible filaments with a width of
157 approximately 15 nm (**Figure 1A**). Using segmented helical reconstruction
158 (Desfosses et al., 2014; Scheres, 2012), we set out to determine the structure of p62
159 filaments. Due to pitch heterogeneity between 130 and 160 Å (**Figure 1B** and
160 **Supplementary Fig. 1B**), we refined a more homogeneous subset with a 137.3 Å
161 pitch and 13.7 units per turn (corresponding to 10.0 Å helical rise and a -26.3° helical
162 rotation) including dihedral symmetry and obtained a 3D reconstruction at 5.3 Å
163 global resolution (**Supplementary Fig. 1C-D, Table 1**). Consistent with the class
164 averages, the local resolution varied significantly from a well-defined PB1 domain
165 scaffold at 4.5 Å resolution up to over 10 Å for the more flexible regions (**Figure 1C**).
166 The cryo-EM structure revealed a left-handed double-helical filament with two
167 antiparallel strands of PB1 domains in the full-length p62 assembly. The atomic
168 model of the PB1 domain of p62 (PDB: 6TGY) fitted well in the best defined scaffold
169 density supporting β-strand separation (**Figure 1D left**). At lower density thresholds,
170 the ZZ domain envelope emerged connected to the PB1 domain albeit at lower
171 resolution (**Figure 1D right**). The densities of the associated C-terminal domains
172 were weak and poorly resolved presumably due to flexibility with respect to the PB1
173 strands. Based on our p62 filament structure, we expanded the domains to match
174 the PB1 density to the experimentally observed helical symmetry assembly (**Figure**
175 **1E**). The resulting p62 double helix architecture is built on the scaffold of the PB1
176 domain generating a major groove that can accommodate the flexible C-terminal
177 part.

178 **Table 1: Cryo-EM structure determination of full-length p62.**

Processing type	Helical segments
Microscope	Talos Arctica 200 keV
Detector	Gatan K3

Magnification	100,000x
Defocus range [μm]	-0.5 to -3.0
Physical pixel size [Å]	0.8389
Total dose [e^-/Å^2]	50
Micrographs	4038
Extraction box size [Å]	352
Overlap [%]	90
Initial no. of segments	5,000,000
Final no. of segments	158,000
Helical symmetry	
Pitch [Å]	137.3
Rise [Å]	10.044
Rotation [º]	-26.3387
Global map resolution (FSC=0.143)/FDR-FSC [Å]	5.3/4.8

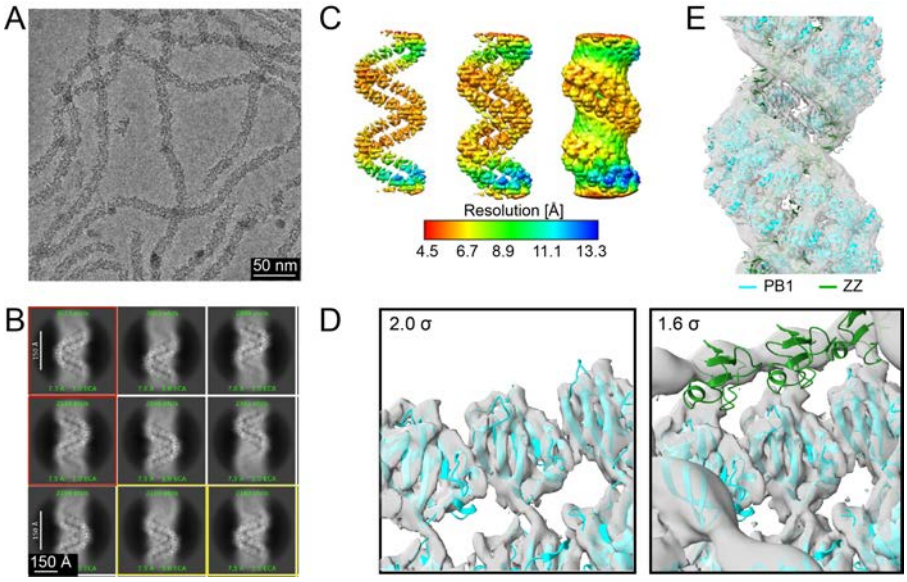

Figure 1: Cryo-EM structure and atomic model of full-length p62 filaments. (A) Representative cryo-micrograph with long and flexible p62 filaments. (B) 2D classes showing well-defined densities of the filamentous scaffold in addition to blur including apparent variation in pitch, with higher helical pitch classes (red frame) and lower helical pitch classes (yellow frame). (C) Three-dimensional density of p62 superimposed with local resolution values showing PB1 domains arranged in a left-handed double helical architecture. The map rendered at different thresholds (2.8 σ, 2.0 σ and 1.4 σ) shows that the PB1 domain is well-resolved (~4.5 Å resolution), the ZZ domain appears as a featureless blob at ~9 Å resolution and the remaining C-terminal domains are not well resolved. (D) Left: The atomic model of the PB1 domain fits well into well-defined PB1 density thresholded at 2.0 σ. Right: The atomic model of the ZZ domain of p62 fits in the featureless blobs seen at lower threshold of 1.6 σ. (E) The atomic model of the helical p62 filament with highlighted PB1 (cyan) and ZZ (green) domains fitted into the filament density displayed at low threshold.

p62 filament interactions with LC3b and ubiquitin

To experimentally study the interactions of p62 filaments with LC3b and ubiquitin, we employed single-particle fluorescence microscopy in total internal reflection fluorescence (TIRF) mode and negative staining EM. We formed p62 filaments at pH=8 and subsequently labeled them at lysine residues with multiple Cy5 dyes (p62 filaments-Cy5) while cyan fluorescent protein (CFP) was fused to LC3b (CFP-LC3b). Consistent with the observed p62 filaments, elongated p62 structures were visible in the Cy5 channel, rather mobile and diffusing above the surface in dilute nM concentrations on the cover slip (**Figure 2A** and **Supplementary Video 1**). Upon addition of equimolar amounts of CFP-LC3b, the same filament became visible in the CFP channel as well (**Figure 2B** and **Supplementary Video 2**) supporting that LC3b was bound to the p62 filaments. Upon addition of GST-4xUbiquitin (GST-4xUb) to the labeled filaments, we observed a rapid and spontaneous formation of μm-sized condensates that displayed minimal mobility (**Figure 2C** and **Supplementary Video**

209 **3**). Interestingly, the subsequent addition of CFP-LC3b to the formed condensates,
210 resulted in the appearance of smaller mobile diffusing fragments (**Figure 2D** and
211 **Supplementary Video 4**).

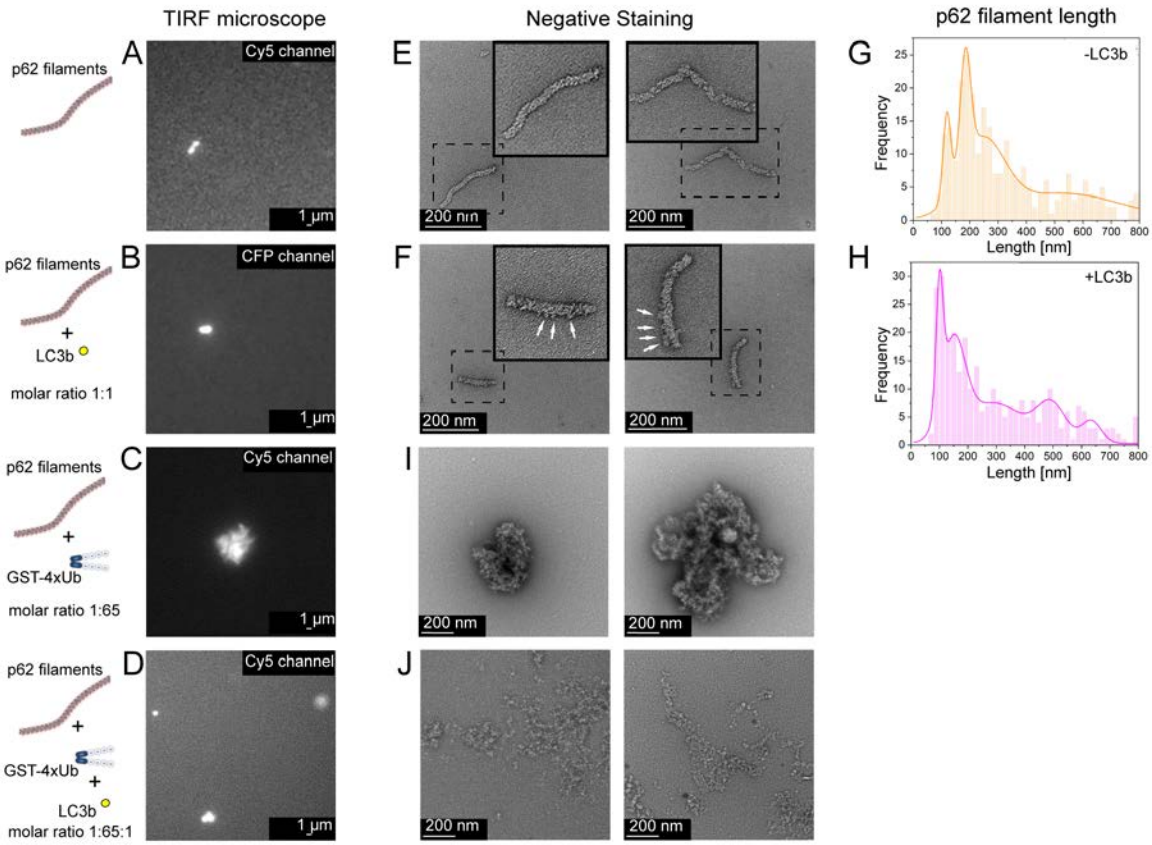

212

213 **Figure 2: LC3b and poly-ubiquitin interactions with p62 filaments visualized by**
214 **single-particle fluorescence and negative staining EM. p62 filament (A) labeled**
215 **with Cy5 on TIRF microscope and (B) in the presence of CFP-LC3b. (C) p62**
216 **condensates forming in the presence of GST4x-ubiquitin (GST4x-Ub). (D) p62**
217 **condensates formed by GST4x-Ub disintegrate after addition of LC3b. (E)**
218 **Negative staining of p62 filaments. Dashed boxes correspond to inset at higher**
219 **magnification. (F) Negative staining of p62 filaments decorated with LC3b (sample**
220 **as in B) (white arrows in inset). Histograms of (G) p62 filament length (H) after**
221 **addition of LC3b. (I) Negative staining of p62 condensates (sample as in D with**
222 **GST4x-Ub). (J) Negative staining of p62 condensates after addition of LC3b**
223 **(sample as in D with GST4x-Ub).**

224 The corresponding p62 filament samples in nM concentration were also imaged by
225 negative staining EM. In the presence of CFP-LC3b, p62 filaments exhibited a
226 distinctive decoration in comparison with the filaments alone (**Figure 2E/F**, white
227 arrows in insets). A quantitative analysis of the filament length distribution revealed a
228 shift towards shorter filaments for CFP-LC3b (**Figure 2G/H**), suggesting that
229 interaction with LC3b induced depolymerization of p62 filaments. Similarly, in the

230 presence of CFP-LC3b, GST-4xUb-induced condensates were disintegrated into
231 smaller substructures (**Figure 2I/J**). In support of previous studies (Sun et al., 2019;
232 Zaffagnini et al., 2018b), our single-particle studies in fluorescence and electron
233 microscopy performed in diluted nM concentration showed that poly-ubiquitinated
234 cargoes induce condensate formation while LC3b can promote disassembly of
235 preformed p62 filaments as well as preformed condensates.

236 In order to molecularly assess the cryo-EM structure and the presented binding
237 experiments, we generated a multimer AI-prediction of p62 using AlphaFold3 (AF3)
238 (Abramson et al., 2024) consisting of ten subunits that formed closed rings mediated
239 by the well-characterized PB1 domain interactions (**Supplementary Fig. 2A**). In an
240 expanded model matching the helical symmetry, the C-terminal UBA domain fits
241 tightly to the major groove next to the PB1 domain that is consistent with the cryo-
242 EM density (**Supplementary Fig. 2B**). When the model is seen in top view, the PB1
243 domain scaffold and UBA domain are located at the outer rim of the filament while
244 the ZZ domain is located on the inside. Notably, parts of the IDR, including the LIR
245 and KIR binding motifs, are positioned towards the filament's outside, supporting the
246 observed molecular access of p62 interacting partners through the major groove of
247 the filament. To assess the interaction accessibility within the p62 filament in more
248 detail, we generated a second p62 multimer model in the above described way, this
249 time with LC3b known to bind to the LIR motif of p62 (Pankiv et al., 2007). In the
250 resulting model, LC3b is tightly fit in the filament's major groove surface between the
251 PB1 domain and covering the UBA domain (**Supplementary Fig. 2C**). The LIR of
252 p62 is positioned outward and bound in the hydrophobic pocket 1 (HP1) and 2 (HP2)
253 of LC3 in agreement with previously determined X-ray structures (Ichimura et al.,
254 2008). A third p62 AF3-model with bound ubiquitin revealed that ubiquitin also
255 resided in the major groove suggesting a competing mode between LC3b and
256 ubiquitin binding. Together, the AF3-based integrative molecular model of the p62
257 filament supports the observed accessibility to binding partners of ubiquitin and LC3b
258 while it also provides a molecular framework for the observed opposing higher-order
259 structures of filament bundling and disassembly.

260 p62 filament membrane interactions

261 In order to more closely mimic the cellular conditions, we performed the interaction
262 studies at higher μM concentrations of p62 and investigated the binding of GST-
263 4xUb and LC3b maleimide-conjugated to small unilamellar vesicles (SUVs).
264 Subsequently, we visualized the natively preserved ultrastructures using cryo-ET. To
265 better characterize the fine ultrastructure of p62 filaments on the image level, we

266 recorded tomograms using the Volta phase plate for detailed high-contrast
267 visualization. The resulting 3D tomograms showed 15 nm-wide flexible p62 filaments
268 consistent with repeating pitches of 14 nm along the filament exhibiting regular major
269 groove indentations matching the pH=6 conditions described above (**Figure 3A**).
270 Closer inspection revealed overlapping filaments crossing underneath each other,
271 branching filaments where individual PB1 scaffold strands are adopting a close to
272 90º bent as well as a cross-over reminiscent of Holliday junctions in double-stranded
273 DNA. Due to the underfocus-induced white halo of phase plate surrounding the
274 filament density, we turned back to conventional cryo-imaging at underfocus and
275 closer to physiological pH 7.4 for the subsequent tomograms. Upon addition of GST-
276 4xUb, p62 filaments were found to concentrate locally by forming bundles of parallel
277 filaments supported by filament image segmentations (**Figure 3B**). Bundle formation
278 was accompanied by the formation of *μ*m-sized 3D agglomerates that were often too
279 thick to be imaged by cryo-ET while visible by negative staining EM (**Supplementary**
280 **Fig. 3**) being consistent with the previous in vitro observations of phase separated
281 p62 bodies (Sun et al., 2019; Zaffagnini et al., 2018b). When we incubated p62
282 filaments with LC3b-conjugated SUVs, we observed unbound filaments as in the
283 p62-only control in proximity to SUVs as well as SUV bound filaments (**Figure 3C**).
284 When not bound, the p62 exhibited the typical filament appearance with a regular 14
285 nm pitch and major groove indentations as well as unwound stretches of the high
286 pH=8 p62 sample alone (**Figure 3D**). When p62 filaments were found connected to
287 the SUV density, they were either laterally associated along the membrane of the
288 SUVs or bound through their ends. As in solution, some laterally associated
289 filaments were characterized by densities giving up the regular helical pitch 14 nm
290 repeat giving rise to more open and unwound stretches. The co-incubation of GST-
291 4xUb and LC3b-conjugated SUVs resulted in less dense network of filament bundles
292 in comparison with GST-4xUb alone as well as SUV bound filaments (**Figure 3E**).
293 Together, the cryo-ET visualization of purified p62 revealed the flexible properties of
294 p62 filaments including cross-overs and branching, bundling of parallel p62 filaments
295 in GST-4xUb bound condensates as well as the lateral association of the helical
296 assembly on the surface of LC3b-conjugated membranes.

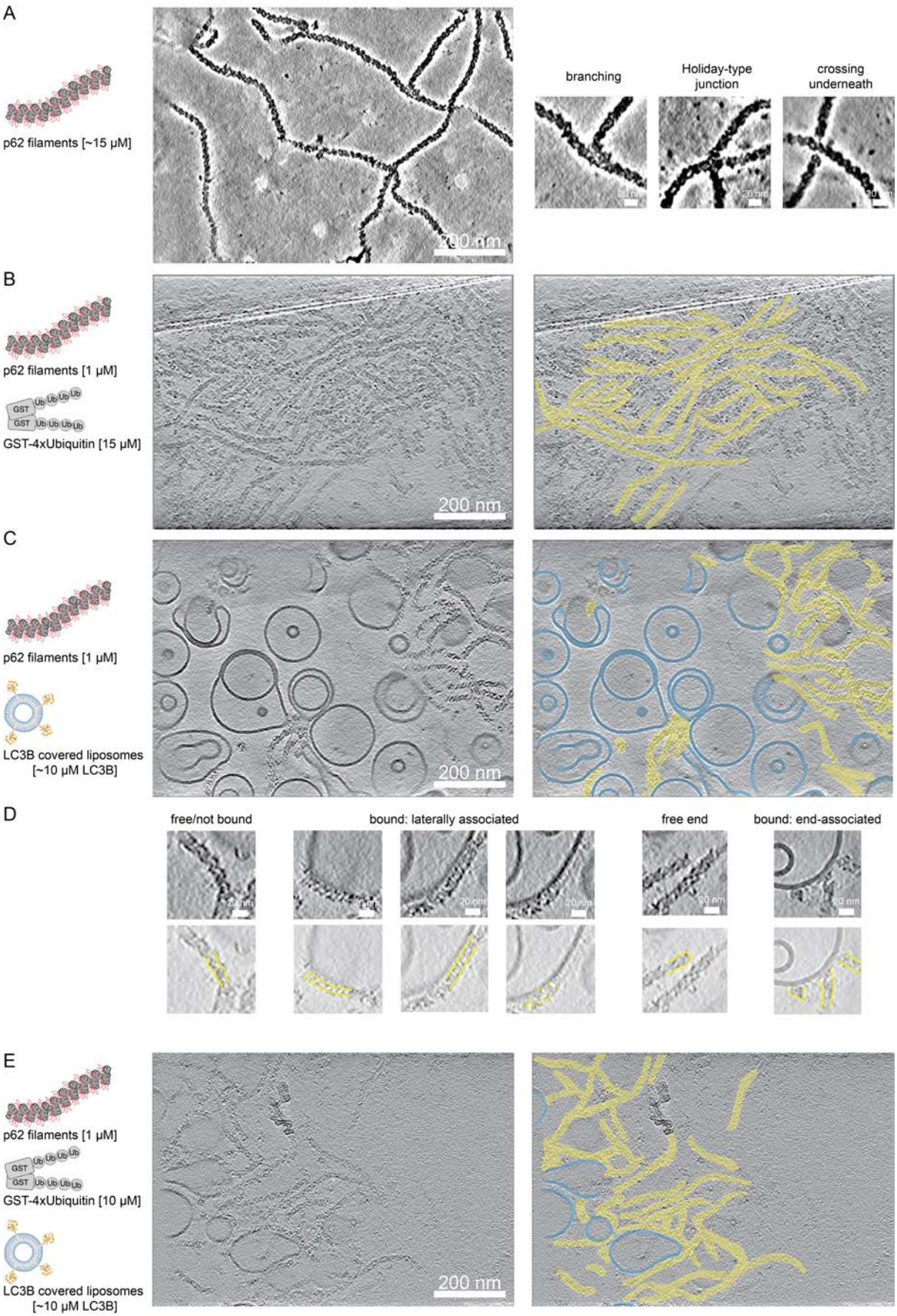
A
p62 filaments [~15 µM]
200 nm
branching
Holiday-type junction
crossing underneath
B
p62 filaments [1 µM]
GST
Ub
GST-4xUbiquitin [15 µM]
200 nm
C
p62 filaments [1 µM]
LC3B covered liposomes [~10 µM LC3B]
200 nm
D
free/not bound
bound: laterally associated
free end
bound: end-associated
E
p62 filaments [1 µM]
GST-4xUbiquitin [10 µM]
LC3B covered liposomes [~10 µM LC3B]
200 nm

297

298 **Figure 3: p62 filament interactions with LC3b-conjugated liposomes and poly-**
299 **ubiquitin visualized by cryo-electron tomography. (A) Left. Representative**
300 **micrograph of p62 filaments recorded with Volta phase plate. Gold fiducials were**
301 **computationally removed in the locations of the smooth circles. Right. Close-up**
302 **insets showing the regular 14 nm pitch features along the filament. p62 filament**
303 **were found crossing each other underneath (left), branching by 90° (center) and**
304 **cross overs as in the Holliday junctions of DNA (right). (B) Left. Upon addition of**
305 **GST-4xUbiquitin, the formation of parallel p62 filament bundles was observed.**
306 **Right. Segmentations of closely packed p62 filaments aligned in parallel. (C) The**
307 **addition of pre-formed p62 filaments to LC3b-conjugated small unilamellar**
308 **vesicles (SUVs) showed bound and unbound p62 filaments. (D) Top. p62 filaments**
309 **were found not-bound (left), bound laterally associated with the membrane (left**
310 **center), free ends (right center) or through their ends (right). Bottom. Outline of**
311 **p62 densities is highlighted in yellow. For laterally associated p62, regular helical**
312 **and unwound assemblies were observed. (E) Co-incubation of GST-4xUbiquitin**
313 **and LC3b-conjugated SUVs led to a dense network of p62 bundled filaments**
314 **partially bound to SUVs.**

315 ATG5 knockdown accumulates co-localized p62 punctae and lipid 316 droplets

317 In order to further our understanding on the structural organization of autophagy
318 receptor p62, we decided to visualize the cargo receptor in cells. Capturing rare and
319 transient p62 punctae is challenging, therefore, we turned to a model system of
320 ATG5 depletion that was shown to increase the size and number of p62 punctae in
321 MEF cells and mice (Morishita et al., 2013; Pankiv et al., 2007) along with increased
322 numbers of lipid droplets (Singh et al., 2009). We stalled autophagy by treating
323 human RPE1 cells stably expressing mCherry-p62 with siRNA against ATG5 for 72
324 hours. To validate the phenotype upon ATG5 knockdown, we detected p62 punctae
325 as well as lipid droplets by confocal fluorescence microscopy using mCherry-p62
326 and the lipid-droplet specific Lipi-Blue dye, respectively, in conditions of no
327 transfection, mock transfection and transfection with ATG5 siRNA (**Figure 4A-C**). As
328 a control for mCherry-p62, we imaged lipid droplets in RPE1 reference cells with
329 Lipi-Blue after no transfection, mock transfection and transfection with ATG5 siRNA
330 using confocal microscopy (**Figure 4D-F**). In order to confirm successful ATG5
331 siRNA knockdown, we performed a Western blot of the RPE1 cells showing a
332 reduction in ATG5 expression levels by 90 % in comparison with the control samples
333 (**Figure 4G**). When incubated with ATG5 siRNA, the number of p62 punctae was
334 highest at an average of 37 per mCherry-p62 RPE1 cell (**Figure 4H**). In the
335 presence of ATG5 siRNA, the average size of the lipid droplets increased from 0.30
336 to about 0.45 μm^2 for mCherry-p62 RPE1 and for RPE1 cells (**Figure 4I**), while we
337 also counted the highest number of co-localized p62 punctae in comparison with no
338 or mock siRNA (**Figure 4J**). Interestingly, in our mock transfected cells we already
339 observed a moderate increase in lipid droplet sizes and p62 punctae possibly due to

the fact that cationic lipid mixtures have been observed to induce autophagy promoting LC3 conversion and p62 degradation (Man et al., 2010; Mo et al., 2012). Together with the autophagy-stalling effect of ATG5 siRNA, they likely contribute to further enrichment of p62 positive structures. In conclusion, when transfecting RPE1 cells with ATG5 siRNA, we observed an accumulation for p62 punctae and lipid droplets as well as a size increase for lipid droplets. The characterized condition of ATG5 knockdown may be well suited for the in situ visualization of p62 punctae as p62 cargo uptake in the lysosome is impaired.

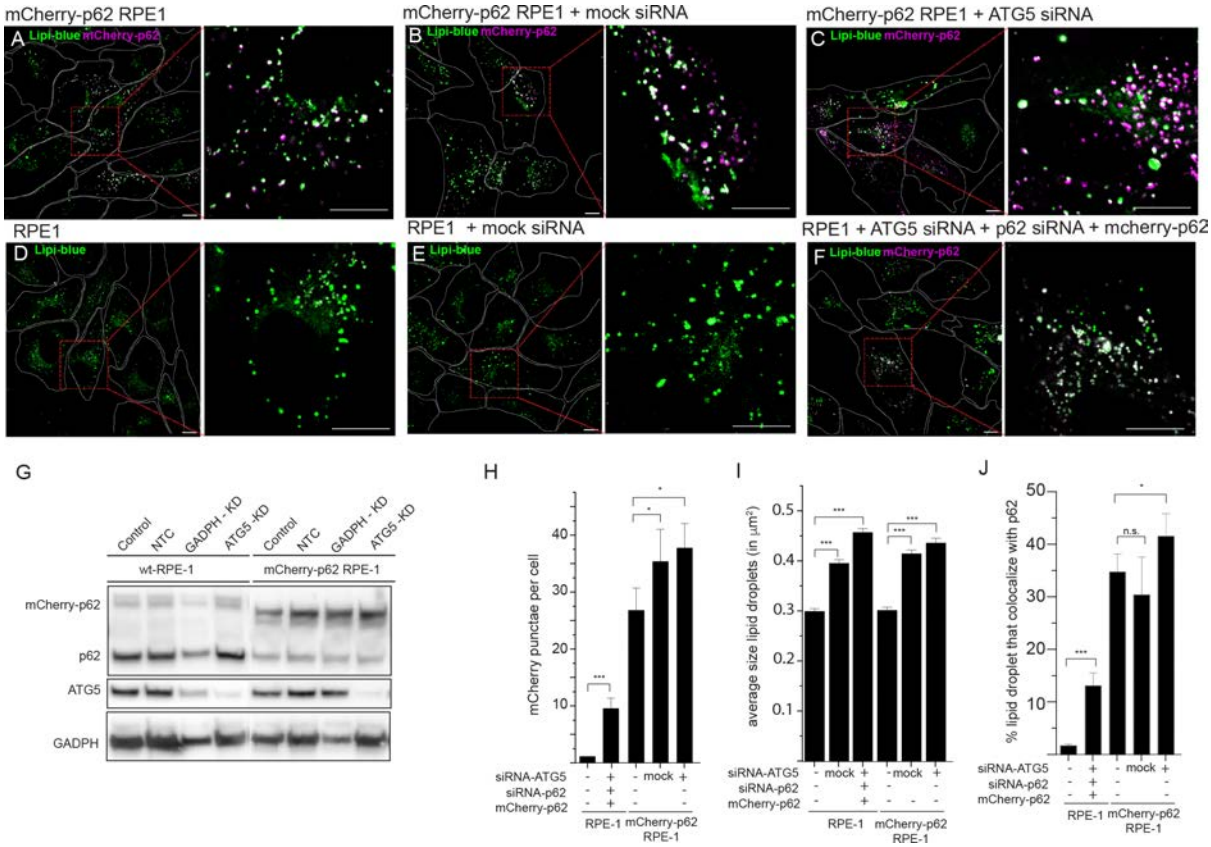

Figure 4: Confocal fluorescence microscopy of p62 punctae and lipid droplets upon ATG5 knockdown. mCherry-p62 RPE1 cells stained with Lipi-Blue for 24 hours at conditions of (A) no transfection, (B) 72 hrs after a mock transfection with RNAiMax and (C) 72 hrs after a transfection with ATG5 siRNA. Reference RPE1 cells stained with Lipi-Blue for 24 hours at conditions of (D) no transfection, (E) 72 hrs after a mock transfection with RNAiMax and (F) 72 hrs after a transfection with ATG5 siRNA. (G) Western blot confirming the knockdown of ATG5 expression including a control knockdown of GADPH. Quantifications for the displayed samples: (H) Number of p62 structures per cell, (I) size of lipid droplets and (J) number of p62 punctae and lipid droplets colocalizations. Statistical significance was determined with a t-test: *=p<0.1, =p<0.01,* =p<0.001

p62 encapsulates lipid droplets by a discontinuous coat of variable thickness

Based on the established condition of accumulated colocalized p62 punctae and lipid droplets, we set out to perform detailed in situ structural analyses to study p62 during lipid droplet cargo recognition. The RPE1 cells were grown under the same conditions described above and placed on micropatterned electron microscopy grids, vitrified, subsequently thinned to ~150 nm using a focused ion beam (FIB) and visualized using a scanning electron microscope (SEM) (**Figure 5A**). To verify that the lamella contained mCherry-p62, we imaged the sample using an integrated cryo-fluorescence microscope and correlated it with the FIB-SEM image (Smeets et al., 2021) (**Figure 5B**). When we visualized these p62 structures using super-resolution cryo-confocal microscopy, they showed circularly resolved mCherry-p62 signal on their rim suggesting the cargo encapsulation by the autophagy receptor p62 (**Figure 5C**). At these sites, a total of 25 tomograms were recorded while those with green autofluorescence from lysosomes were not further analyzed. In the reconstructed tomograms, we identified characteristic structures made of a homogeneous texture of spherical shape suggestive of a lipid droplet (Ganeva et al., 2023) (**Figure 5D**) in agreement with the frequent co-localization of p62 and lipid droplet punctae demonstrated above. A dark and highly dense layer was found surrounding the droplet in addition to a single phospholipid bilayer. The homogeneously textured spheres were similar in size measuring between 510 - 530 nm (**Figure 5E**). The surrounding layer, or coat, varied in thickness within a single structure as well as between structures ranging between 4 and 27 nm, with a mean of 12.6 nm (**Figure 5F** and **Supplementary Figure 4**). The distance between the surface of the sphere and the surrounding single lipid membrane was relatively uniform at 13.8 nm with some weaker protein densities filling this space while other densities connecting these two structures (**Figure 5G/H**). The segmented tomograms revealed that when the layer was thin, patches or islands of dark contrast were found distributed around the surface of the lipid droplet (**Supplementary Figure 5**). However, when the layer was thick, it was completely continuous. Next to the lipid droplet, several small vesicles between 35 and 52 nm in diameter were observed consistent with previously described ATG9A vesicles (Mailler et al., 2021). In summary, ATG5 knockdown in human RPE1 cells yielded p62 positive spherical structures of 500 nm diameter composed of an inner lipid droplet and a p62-containing, dense layer of variable thicknesses covering the surface surrounded by a single bilayer membrane.

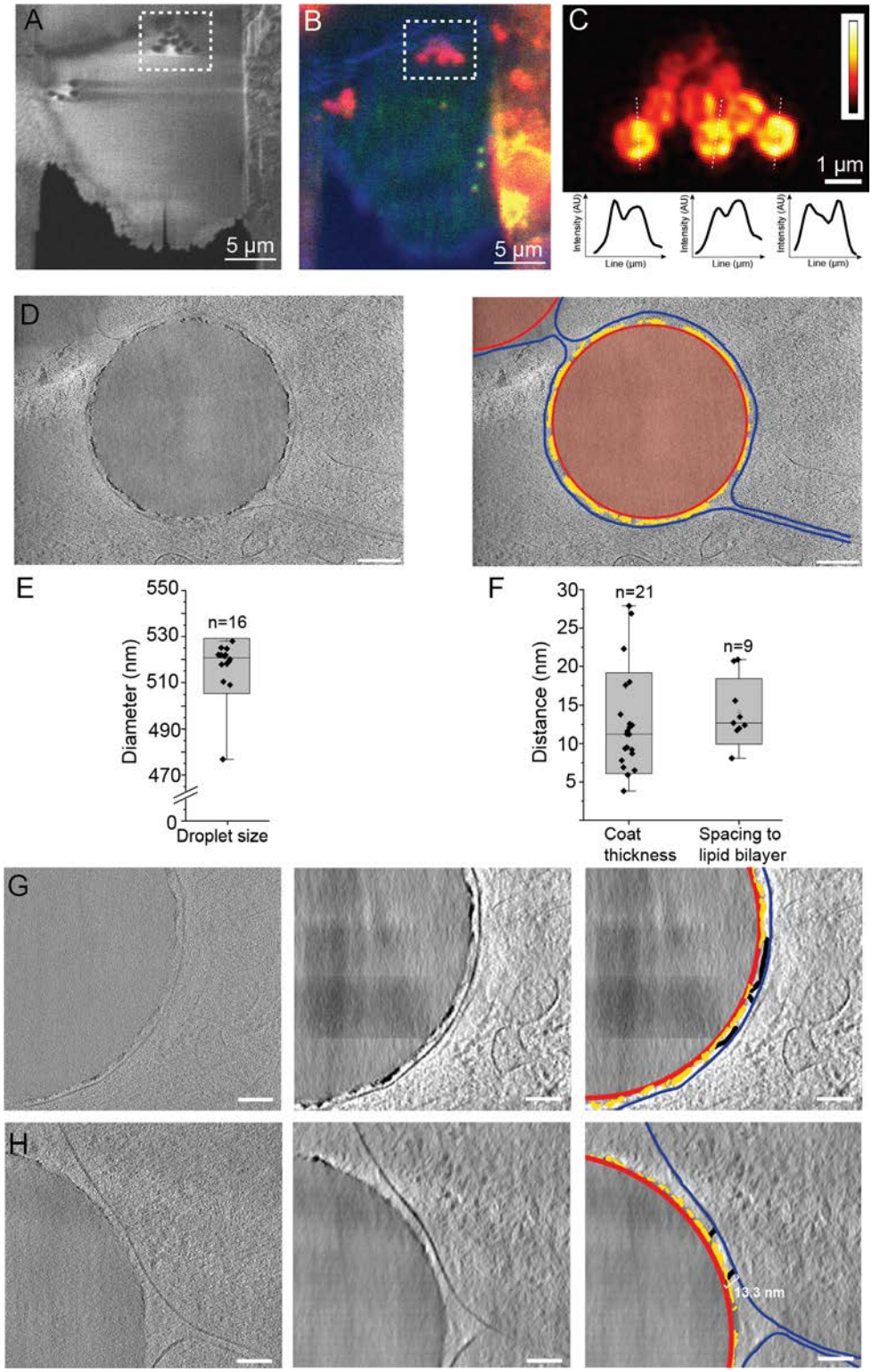

Figure 5: Ultrastructural in situ characterization of p62-encapsulated lipid droplets. (A) Scanning electron microscopy image of a lamella generated from an EM grid grown with RPE1 cells. (B) Correlated fluorescence image of the corresponding lamella recorded with a reflected light channel and fluorescent channels of 595 nm for mCherry-p62 and 515 nm for autofluorescence. (C) Super-resolution cryo-confocal fluorescence image recorded at 561 nm for mCherry-p62 showed three p62-positive structures resolving a circular fluorescence signal as displayed in three corresponding intensity profiles below. (D) Tomographic gray-

scale z-slice through the homogeneous density sphere surrounded by a dark high-contrast layer with an enwrapped single membrane. Scale bar 100 nm. (E) Segmented and labeled structure superimposed on gray-scale z-slice, light red: lipid droplet with red: droplet surface, yellow: dark and high-contrast surrounding p62 layer and blue: single lipid membrane. (F) Left. Box plot indicates a well-defined lipid droplet diameter of about 520 nm. Right. Box plot of measured distances of observed dark layer thickness and spacing of droplet surface to enwrapped single lipid bilayer. (G) Tomographic z-slice of half a lipid droplet in raw grayscale (left), denoised grayscale (center) and superimposed labeled structures of droplet surface (red), dark layer (yellow), weaker protein density (black) and enwrapping single lipid bilayer (blue). Scale bar 50 nm. (H) Tomographic z-slice of another droplet showing the spacing of 13.3 nm between droplet surface and single lipid bilayer. Scale bar 50 nm.

Elemental analysis reveals calcium and phosphorus in the p62 positive layer

Given the strong observed intensity of the surrounding p62-positive layer with respect to the grey levels of the lipid droplet and cytosol, we wondered whether non-organic elements contributed to the high contrast. To address this question, we employed scanning transmission electron microscopy (STEM) coupled with energy-dispersive X-ray (EDX) spectroscopy to record element-specific X-rays from the mCherry-p62 RPE1 lamella treated with ATG5 siRNA investigated above (**Figure 6A-D**). For this sample, we acquired STEM images on a high-angle annular dark-field (HAADF) detector and simultaneously recorded the back-scattered EDX signal (**Figure 6E**). The EDX signal was averaged over the excised regions of the cytosol, lipid droplet core and the p62 coat (**Supplementary Figure 6**). For the cytosol, we detected mostly carbon (C), nitrogen (N) with low and oxygen (O) with high intensity at approx. 300, 400 and 500 eV, respectively. For the lipid droplet, we observed enriched C in comparison with the cytosol, reduced N and O consistent with the presence of triacyl glycerides and sterols within the sphere of lipid droplets. In both regions, no inorganic elements were observed at higher energies. For the p62 coat, we found the C, N, O signal comparable to the cytosol with clear additional inorganic signals of magnesium (Mg), calcium (Ca) and phosphorus (P) at 1250, 2000 and 3800 eV, respectively, supporting the observation of the relatively strong contrast in the raw tomograms. The detected high levels of Ca and P suggest the presence of calcium phosphate. As a control, we focussed on lipid droplets showing no p62 colocalization and obtained a very similar EDX signal (**Supplementary Figure 7**). Other p62 positive single-membrane vesicular structures resembling lysosomes showed no differences in EDX profiles between the vesicular area and the cytosol (**Supplementary Figure 8**).

443 Given the unexpected finding of inorganic elements located in the p62 coat, we
444 tested whether the addition of Ca^{2+} ions had an effect on purified p62 filaments.
445 When increasing the $CaCl_2$ concentrations from 100 nM to 100 mM, we observed a
446 bundling of p62 filaments at 100 mM $CaCl_2$ in negative staining EM (**Figure 6F-H**).
447 Moreover, when testing other divalent cations such as Zn^{2+} and Mg^{2+}, we found that
448 the addition of $ZnCl_2$ had a stronger clustering effect already visible at 100 μM, while
449 the addition of $MgCl_2$ did not show a significant bundling (**Supplementary Figure 8**).
450 Together, these experiments show that the observed p62-positive structures
451 correspond to lipid droplets surrounded by a coat made of p62, including significant
452 amounts of calcium (**Figure 6I**) that also promotes the formation of p62 oligomer
453 bundles in vitro and may explain the characteristic dense layer observed in the
454 tomograms.

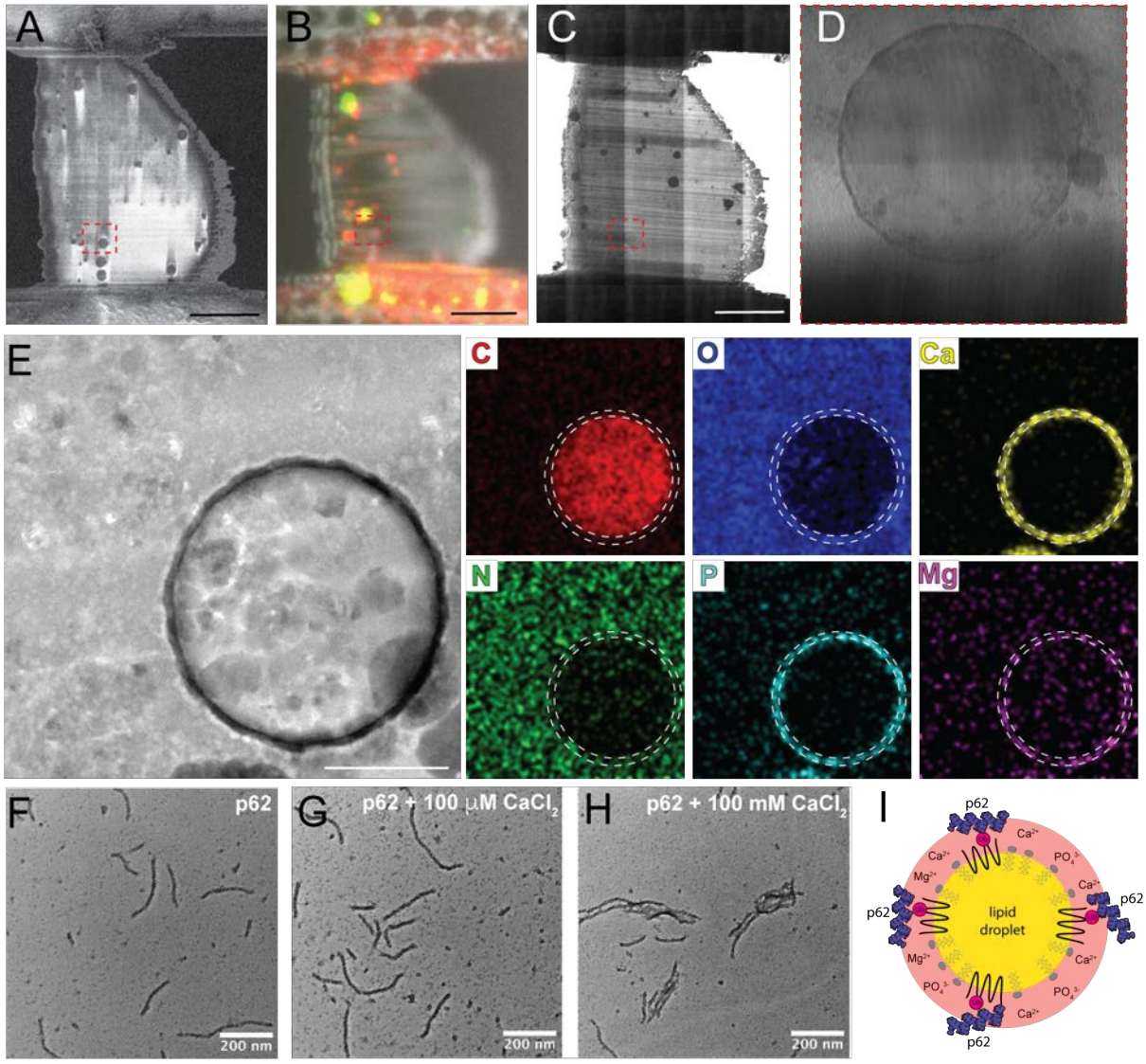

455

456 **Figure 6: Compositional elemental analysis of p62-encapsulated lipid droplets**
457 **using energy dispersive X-ray (EDX) spectroscopy. (A) Scanning electron**

microscopy (SEM) image of milled lamella with inset of characterized lipid droplet. (B) Correlated SEM image superimposed with a reflected light channel and fluorescent channels of 595 nm for mCherry-p62 and 515 nm for autofluorescence. (C) Transmission electron microscopy image of corresponding lamella. (D) Enlarged image of p62-positive lipid droplet. (E) High-angle annular dark-field scanning transmission electron microscopy (HAADF-STEM) image of droplet of interest with corresponding EDX signals for Carbon in red (C), Oxygen in blue (O), Calcium in yellow (Ca), Nitrogen in green (N), Phosphorus in cyan (P) and Magnesium in purple (Mg). Scale bar 500 nm. Negative stain EM images of (F) purified p62 filaments, (G) with 100 μM $CaCl_2$ and (H) 100 mM $CaCl_2$. (I) Model summary of analyzed p62 droplet structures: the lipid droplet devoid of any phospholipids is encapsulated by p62-positive layer that is rich in $CaPO_4$.

Discussion

In the current study, we addressed the structural organization of the archetypical autophagy receptor p62/SQSMT1 at various levels of resolution. Initially, we determined the cryo-EM structure of full-length p62 at 5.3 Å global resolution revealing the double helical filament PB1 scaffold with peripheral lower-resolution densities corresponding to the ZZ-domain and C-terminal part (**Figure 1**). Interestingly, the addition of LC3b led to a shortening of the filament at higher concentrations while GST-4xUb resulted in the bundling of filaments to phase-separated entities consistent with solvent-exposed accessible binding sites to LC3b and ubiquitin through the major groove of the filament (**Figure 2**). When p62 filaments were bound to LC3b-conjugated SUVs, we observed a lateral association on model membranes of the p62 filament while maintaining regular p62 oligomer arrays (**Figure 3**). Moreover, we visualized p62 structures in cells using fluorescence light microscopy, correlative light and electron microscopy (CLEM) followed by cryo-ET in a p62-enriched phenotype due to ATG5 knockdown (**Figure 4 and 5**). The detailed ultrastructural analysis of this autophagy-stalled phenotype revealed a high-contrast layer of p62-positive structures surrounding lipid droplets due its enriched calcium phosphate content (**Figure 6**).

In contrast to the previously determined PB1 assemblies (Jakobi et al., 2020), the here determined full-length p62 filament structure formed a double-helical filament architecture widely known from the classical DNA double helix model (Watson & Crick, 1953). The full-length structure revealed two well-resolved antiparallel PB1 scaffold strands while the PB1 domain-only assemblies have one or two additional PB1 strands inserted into the helical assembly leading to an almost closed tube. In the full-length structure, the space required by the additional 340 C-terminal amino acids restricts the assembly to two antiparallel PB1 strands leaving space for a major groove. Our binding assays showed a shortening the filament upon LC3b interaction

497 in agreement with model predictions of the LIR motif to be accessible in solution
498 through the major groove. In our solution studies, we also found the p62
499 concentrations to be critical for detecting clear binding effects such as shortening or
500 filament bundling in the case of 4xGST-Ub. In addition, we also observed bundling of
501 p62 filaments upon addition of divalent cations in $CaCl_2$ and $ZnCl_2$ solutions (see
502 **Figure 6G-H**). Multivalency available in a polymer and across polymers may mediate
503 the bundling, e.g., when several UBA domains from different filaments bind to
504 polyubiquitin or when parts of ZZ-domains originating from multiple p62 filaments
505 share the coordination of divalent cations such as Zn^{2+} and Ca^{2+}. Multivalent
506 interactions mediated by GST4xUb have been shown to promote phase separation
507 of p62 (Zaffagnini et al., 2018a). In the cell, we expect some of these interactions to
508 be present on membrane surfaces through membrane-linked p62 polymers and
509 oligomers, which provides the principal benefit of high local concentrations offered
510 for low-affinity interactions to be enhanced by high avidity binding. In support of this
511 concept, when we linked the binding partner LC3b (Pankiv et al., 2007) to the
512 liposome membrane surface, upon p62 filament addition we did not observe a
513 complete filament disassembly, rather we observed a lateral binding of the filament.
514 In the images at physiological pH, we also found an unwinding and structural
515 opening up of the double-helical filament architecture located on the membrane
516 surface. In such an assembly configuration, previously inaccessible available binding
517 sites in the interior will become accessible in an opened p62 “bubble” structure while
518 still maintaining functional polymers and oligomers. The unwinding, structural
519 opening and re-arrangement of the filament architecture on membrane surfaces may
520 provide a higher level of regulating access of binding partners to the multiple binding
521 sites in p62.

522 After the in vitro structural and biochemical work, we turned to the RPE1 cellular
523 model to investigate the ultrastructural details of p62 using cryo-ET. In order to
524 enrich p62 structures, we depleted ATG5 that is an essential member of the core
525 machinery driving autophagy progression (Mizushima et al., 2001; Morishita et al.,
526 2013; Pankiv et al., 2007). During autophagy, ATG5 is covalently linked to ATG12
527 that together with ATG16L is required for LC3-I conjugation to the membrane in the
528 form of LC3-II and thereby accomplishing phagophore expansion (Otomo et al.,
529 2013). Upon ATG5 depletion, characteristic LC3 punctae and autolysosomes cannot
530 form leading to an accumulation of cargo, e.g., when lipid droplet breakdown is
531 inhibited, triacylglycerides have been shown to accumulate (Singh et al., 2009).
532 Moreover, in mice, ATG5 knockouts have severe consequences for neuronal

533 development leading to delays in maturation as ATG5 appears to be essential for the
534 survival of adult-generated neurons (Xi et al., 2016). Based on the near-native
535 visualization using in situ cryo-CLEM in RPE1 cells, we observed p62-positive
536 structures wrapping around lipid droplets made of triacylglycerides giving rise to
537 homogeneous density in the electron tomograms and characteristic EDX signals.
538 Lipid droplets have been observed in the diameter ranges of 100 nm to over 1 µm in
539 size (Schott et al., 2019) while the here observed ones had relatively narrow
540 distribution of 500 to 540 nm. Lipophagy has been described as being initiated by the
541 ubiquitination of PLIN proteins embedded in the phospholipid monolayer surrounding
542 the lipid droplets (Tsai et al., 2017). Moreover, LC3 and p62 were also described as
543 forming punctae on the surface of lipid droplets (Robichaud et al., 2021). In this way,
544 they are thought to induce the formation of the autophagosomal membrane
545 surrounding the lipid droplets. While in ATG5 depleted cells LC3-II is not present on
546 the membrane, p62 has been shown to still be capable of recruiting cargo, ATG9A
547 vesicles, ATG16L vesicles and FIP200 condensates (X. Feng et al., 2023; Itakura &
548 Mizushima, 2011). Possibly, the small vesicular structures we observed next to the
549 p62 positive lipid droplets (see **Supplementary Figure 5B**) may correspond to
550 previously observed ATG9 vesicles (30-60 nm) or ATG16L vesicles (Dupont et al.,
551 2014; Mailler et al., 2021; Puri et al., 2013; Yamamoto et al., 2012).

552 When we segmented tomography data of the ATG5 depleted cells, we observed p62
553 coating of various thicknesses on the lipid droplets. In close vicinity, we often found a
554 single, unclosed membrane (see **Supplementary Figure 5A**) enwrapping the coated
555 lipid droplet. In the ATG5 knockdown condition, we do not expect a bona fide
556 autophagy double membrane to be present. Due to the observed connections to
557 membrane stacks, it appears plausible that we visualized recruited ER membrane
558 unable to extend and seal off the lipid droplets due to the lack of lipidated LC3-II. In
559 our p62-positive structures, we also observed 13.3 nm wide protein density
560 connecting the droplet surface/coat and the enwrapped membrane in addition to
561 elongated flexible density. The density is not compatible with regular helical p62
562 filaments used for structure determination above as no pitch repeat distance along
563 the long axis is discernible. Alternative assemblies, however, such as unwound or
564 opened p62 filaments share similar width dimensions to the measured 13.3 nm.
565 Other potential molecules of the autophagy core machinery include ATG2A/B (Y.
566 Wang et al., 2024), the ULK1 complex (Chen et al., 2023) or FIP200 (Chen et al.,
567 2023) all of which have elongated shapes but are either longer or shorter than the
568 observed densities. Clearly, more research and improved imaging features will be

569 required to confirm the identity of the protein complexes involved in the studied p62-
570 positives structures.

571 The p62-lipid droplet structures we have visualized in this study were found
572 surrounded by dark layers. We identified them to be mainly composed of calcium,
573 phosphorus and magnesium using EDX spectroscopy suggesting high levels of
574 calcium phosphate. Previously, the same approach has been used on vitreous
575 sections and other frozen hydrated samples (Kumar et al., 2020; WOLF et al., 2015;
576 Wolf et al., 2017; Zierold et al., 1984) while in this study we employed it on FIB-
577 milled lamella. A dark high-contrast layer had been observed before in close
578 proximity to lipid droplets in the context of autophagy using plastic section electron
579 microscopy (Robichaud et al., 2021; Schott et al., 2019; Singh et al., 2009). We do
580 not claim that the previously imaged structures correspond to structures we
581 observed, nevertheless the resemblance is noteworthy. For some time, intracellular
582 calcium levels have been linked to autophagy as rapamycin-induced autophagy led
583 to an increase in cytosolic Ca^{2+} concentration and a decrease in the calcium ER leak
584 rate both of which were independent of LC3 lipidation (Decuypere et al., 2013).
585 Moreover, the addition of a calcium chelator such as BAPTA-AM was shown to be
586 sufficient to block autophagy initiation (MacVicar et al., 2015). In a more recent
587 study, evidence was provided that brief calcium transients are released from the ER,
588 which trigger FIP200 punctae formation and modulate phase separation at the
589 autophagosome assembly site (Q. Zheng et al., 2022). In yeast, calcium has also
590 been shown to be required for autophagy initiation under glucose starvation
591 conditions (Yao et al., 2024). It seems plausible that in this study we directly
592 observed calcium ions bound to the lipid droplet surface originally released from the
593 ER, which help to organize the early stages of lipophagy. Given the demonstrated
594 bundling capabilities of p62 by divalent cations in solution, it is possible that the
595 observed dark p62-positive coat found on the cargo lipid droplet is the result of
596 calcium transients release from the ER that orchestrate the early stages of
597 autophagy machinery recruitment. Further research will be required to fully establish
598 the links between the here presented cryo-EM structure, biochemical binding
599 properties, higher-order organization, in situ ultrastructure and autophagy initiation.

600

Supplementary Figures

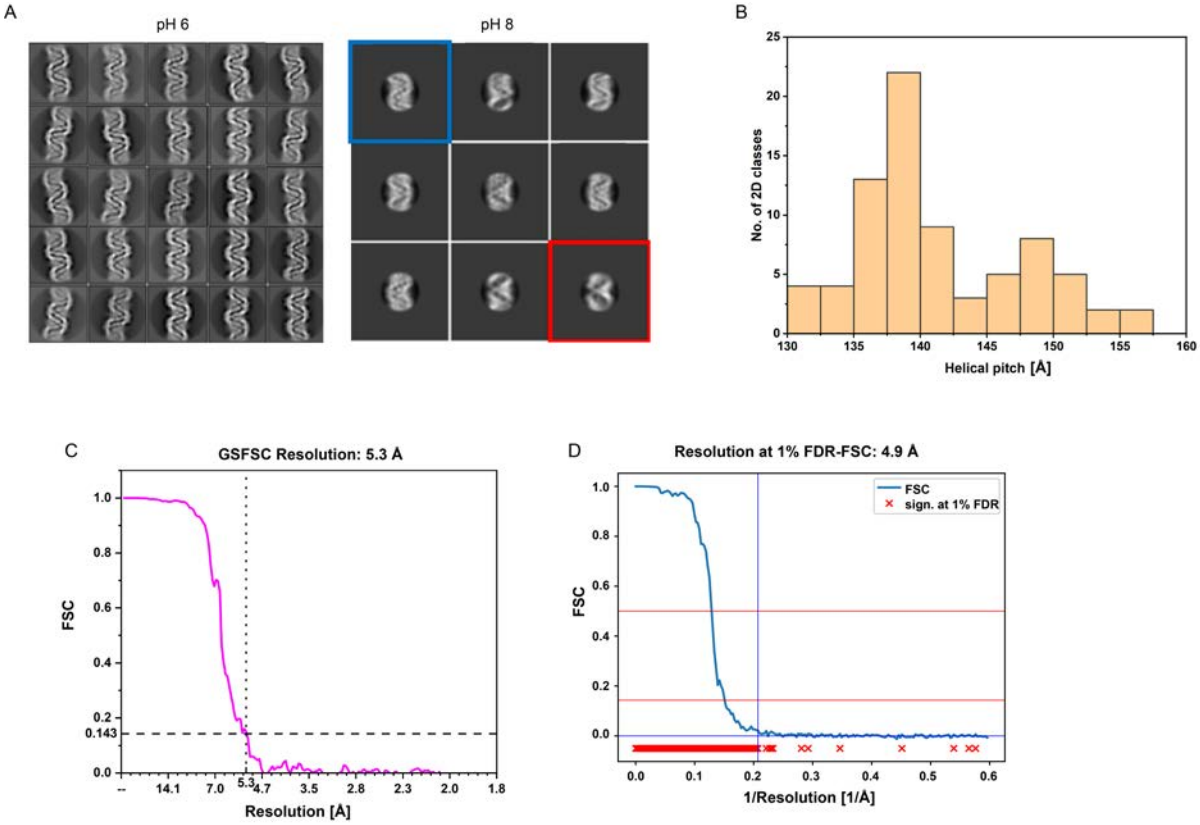

Supplementary Figure 1: p62 filament sample optimization, helical pitch of p62 filaments and resolution assessment of p62 cryo-EM structure. (A) 2D classification at pH 6 (left) and pH 8 (right). At pH 6, the classes show a regular helical architecture. At pH 8 almost 60% of the particles show an unwinding of the two strands (red), whereas 40% of the particles still show a closed form of the filament (blue). (B) Helical pitch distribution of p62 filaments ranges from 130 to 160 Å. (C) Fourier shell correlation (FSC) curve of the p62 filament density map indicates a resolution according to the cutoff FSC(0.143)=5.3 Å. (D) FDR-FSC curve indicates a resolution of 4.8 Å.

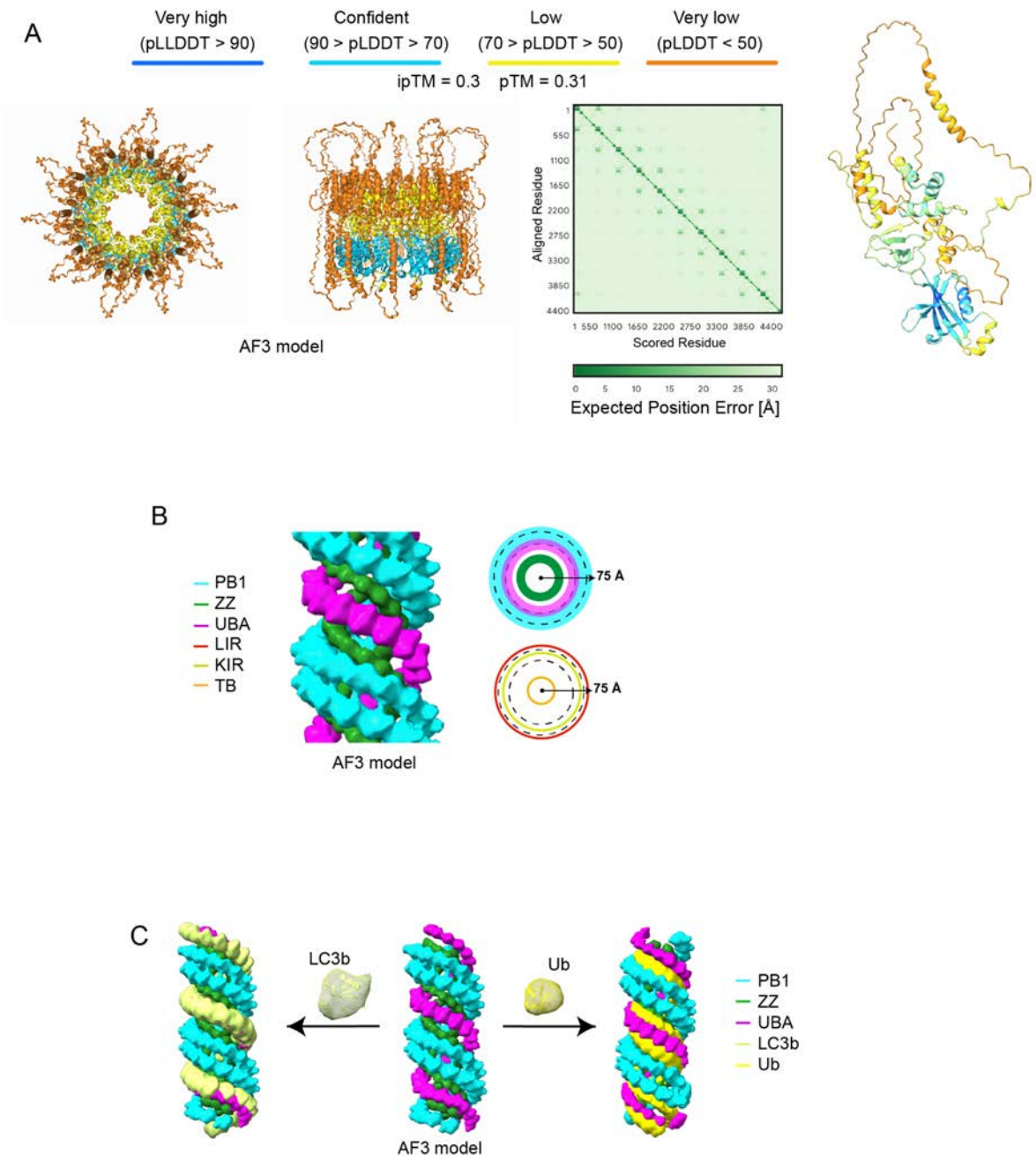

Supplementary Figure 2: AlphaFold3 prediction of p62 assembly, domain localization, binding of LC3b and competition with ubiquitin. (A) Left. AlphaFold3 (AF3) model of the p62 decamer ring (top and side view), colored according to a per-atom confidence estimate. Predicted aligned error (PAE) plot reveals spatial proximity of the domains. Right. Single p62 molecule AF3 prediction excised from 10-mer colored with per-residue model confidence estimate. (B) p62 filament model of AF3 predictions showing PB1 (cyan), ZZ (green) and UBA (magenta) domains rendered at 15 Å resolution. Top views showing relative position of subunits and binding sites and their radial distance from the center of the filament.

The two dotted lines mark the position of the PB1 domain that corresponds to the strongest observed density in the cryo-EM map. (C) p62 filament models of AF3 predictions rendered at 15 Å resolution with LC3b (left) or ubiquitin (right) bound.

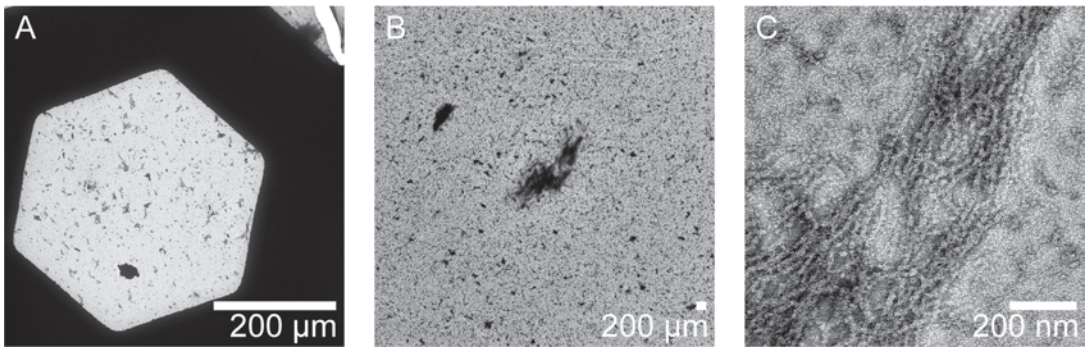

Supplementary Figure 3: Phase separation of p62 filaments induced by addition of GST-4xUbiquitin. p62 filaments at 1 μM concentration were mixed with 15 μM GST-4xUbiquitin, incubated for four minutes and subsequently negatively stained. The resulting phase separation droplets were imaged at (A) 100x, (B) 8,500x and (C) 57,000x magnification revealing dense clusters of p62 filament bundles.

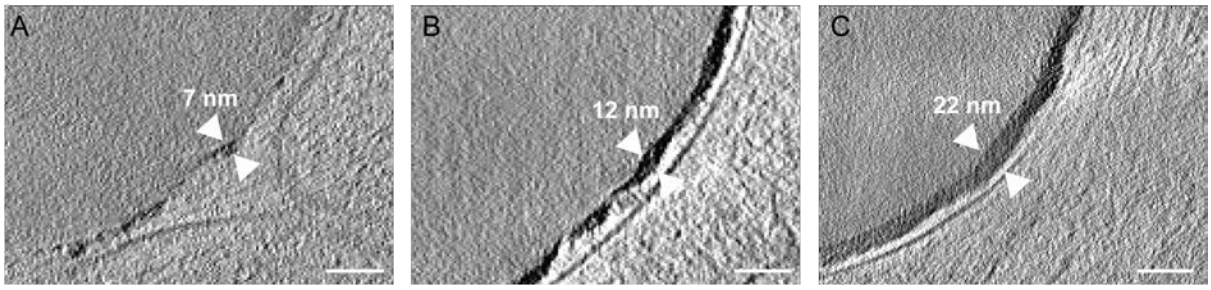

Supplementary Figure 4: Different thicknesses of droplet coats. Lipid droplets are coated by a high-contrast layer of different thicknesses measuring (A) 7 nm, (B) 12 nm and (C) 22 nm. Scale bar 50 nm.

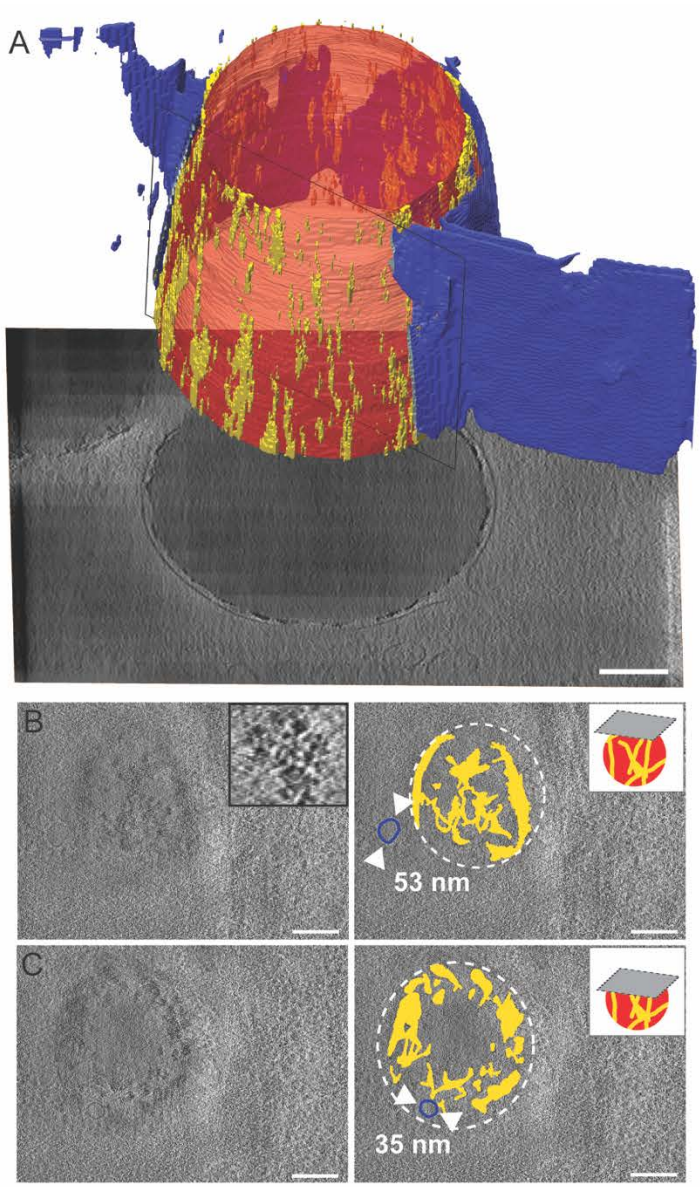

Supplementary Figure 5: Segmented tomogram showing a thin discontinuous high-contrast p62-positive coat surrounding the lipid droplet. (A) Segmented tomogram rendered in three dimensions: lipid droplet (red), p62-positive coat (yellow) enwrapped by a single lipid bilayer stack (blue). The membrane was opened up using a clipping plane (black rectangle) for easier visualization. (B) Upper z-section through segmented tomogram reveals the thin discontinuous surface coating around the lipid droplet. Inset shows the granular nature of the surface coating. (C) Center z-section of the same lipid droplet. Small vesicular structures (blue) of 35 and 53 nm diameter are also visible in both z-slices. Scale bar 100 nm.

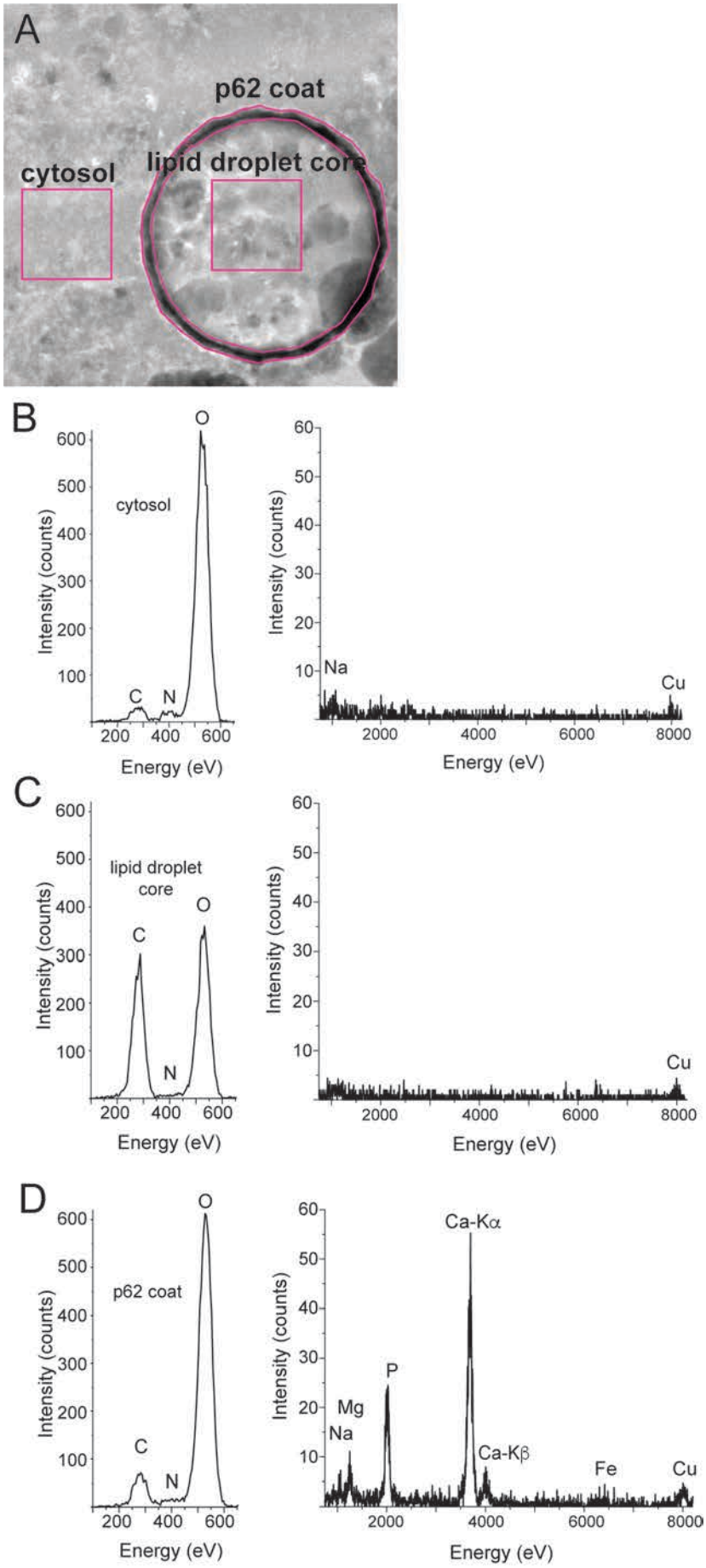
A
p62 coat
cytosol
lipid droplet core
B
cytosol
O
C
N
Intensity (counts)
Energy (eV)
Na
Cu
C
lipid droplet core
O
C
N
Cu
D
p62 coat
O
C
N
Ca-Kα
P
Mg
Na
Ca-Kβ
Fe
Cu

646

647 **Supplementary Figure 6: Energy-dispersive X-ray (EDX) spectroscopy**
648 **combined with STEM imaging of p62-positive lipid droplets.** (A) HAADF-STEM
649 image of p62 positive lipid droplets. Insets indicate the regions used for summing of
650 EDX signals. The same number of pixels were summed in all regions. X-ray spectra
651 showing which elements are present in the different areas; in (B) cytosol, (C) lipid
652 droplet core and (D) dense p62 positive coat, respectively. Peaks were marked with
653 their respective elements. The weak copper (Cu) peak originates from the copper
654 sample holder used.

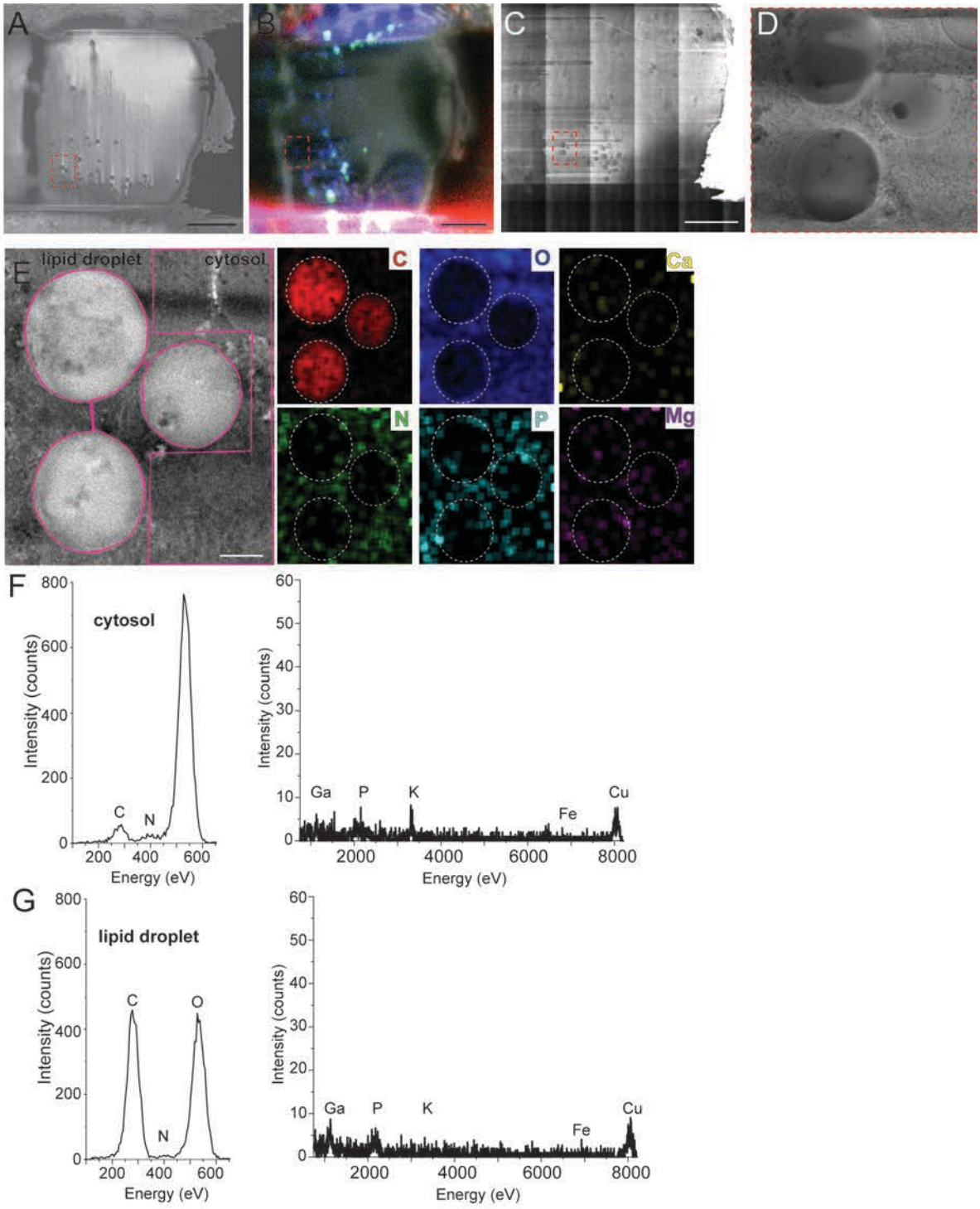

Supplementary Figure 7: Energy-dispersive X-ray spectroscopy (EDX) combined with STEM imaging of native lipid droplets. (A) Scanning electron microscopy images of lamella with visible droplets in inset. Scale bar 5 μm. (B) SEM image superimposed with fluorescent image of Lipi-Blue dye. (C) Overview image of corresponding recorded transmission electron microscope (TEM). (D) Three spatially close lipid droplets in higher magnification TEM image. (E) HAADF-STEM image of three adjacent lipid droplets corresponding elemental images of carbon (C), oxygen

(O), calcium (Ca), nitrogen (N), phosphorus (P) and magnesium (Mg). The image shows two insets of the cytosol and droplet region used for subsequent averaging. EDX spectra of (F) cytosol region and (G) lipid droplet regions. Scale bar 200 nm.

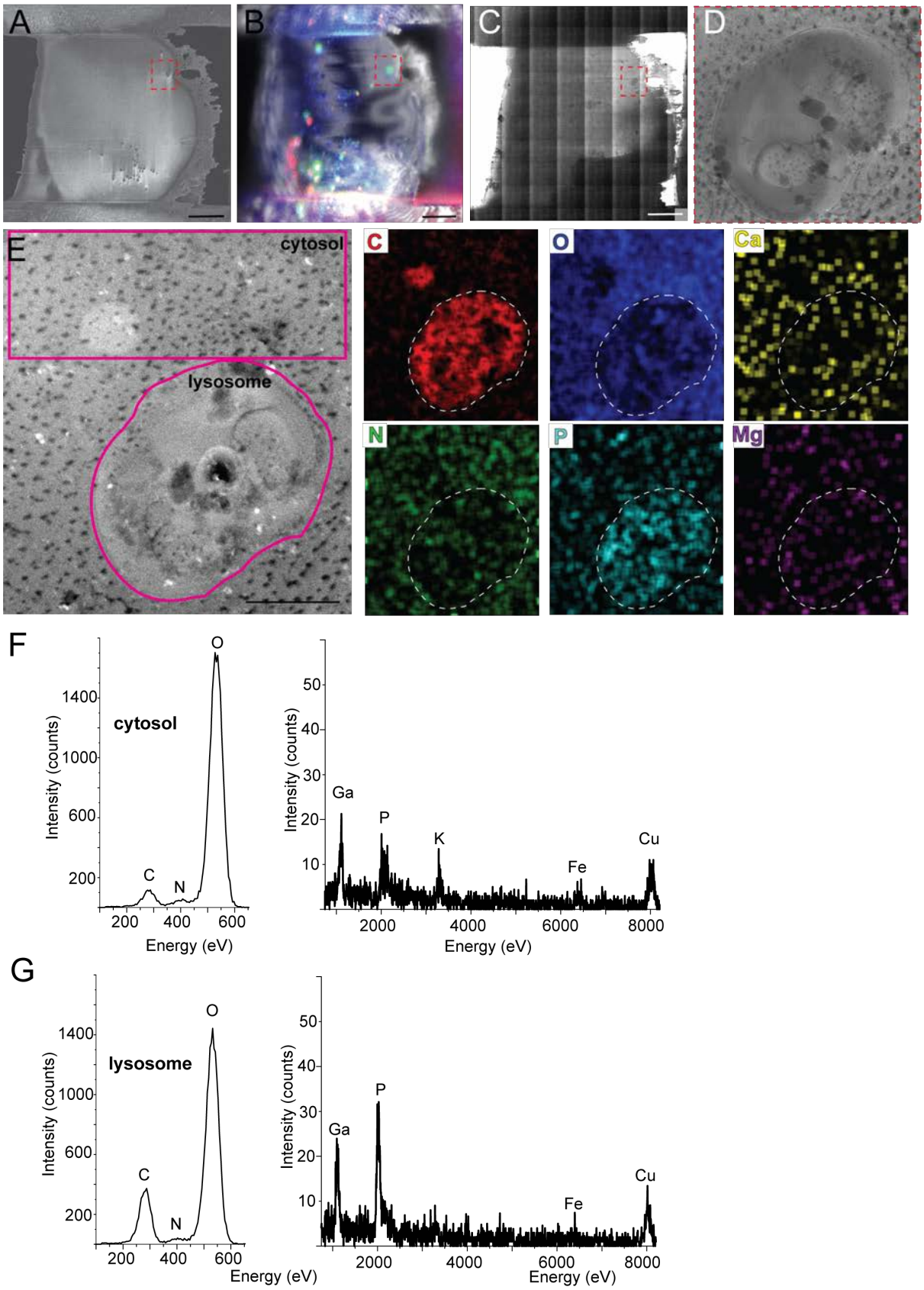

667 **Supplementary Figure 8: Energy-dispersive X-ray (EDX) spectroscopy**
668 **combined with STEM imaging of a lysosome.** (A) Scanning electron microscopy
669 (SEM) images of lamella with visible droplets in inset. (B) SEM image superimposed
670 with fluorescent image of green autofluorescence. (C) Overview image of
671 corresponding recorded transmission electron microscope (TEM). (D) Large
672 vesicular lysosome structure in higher magnification TEM image. (E) HAADF-STEM
673 image of lysosome corresponding elemental images of carbon (C), oxygen (O),
674 calcium (Ca), nitrogen (N), phosphorus (P) and magnesium (Mg). Scale bar 500 nm.
675 The image shows two insets of the cytosol and droplet region used for subsequent
676 averaging. EDX spectra of (F) cytosol region and (G) lysosome regions show
677 significant gallium signal originating from the FIB preparation procedure.

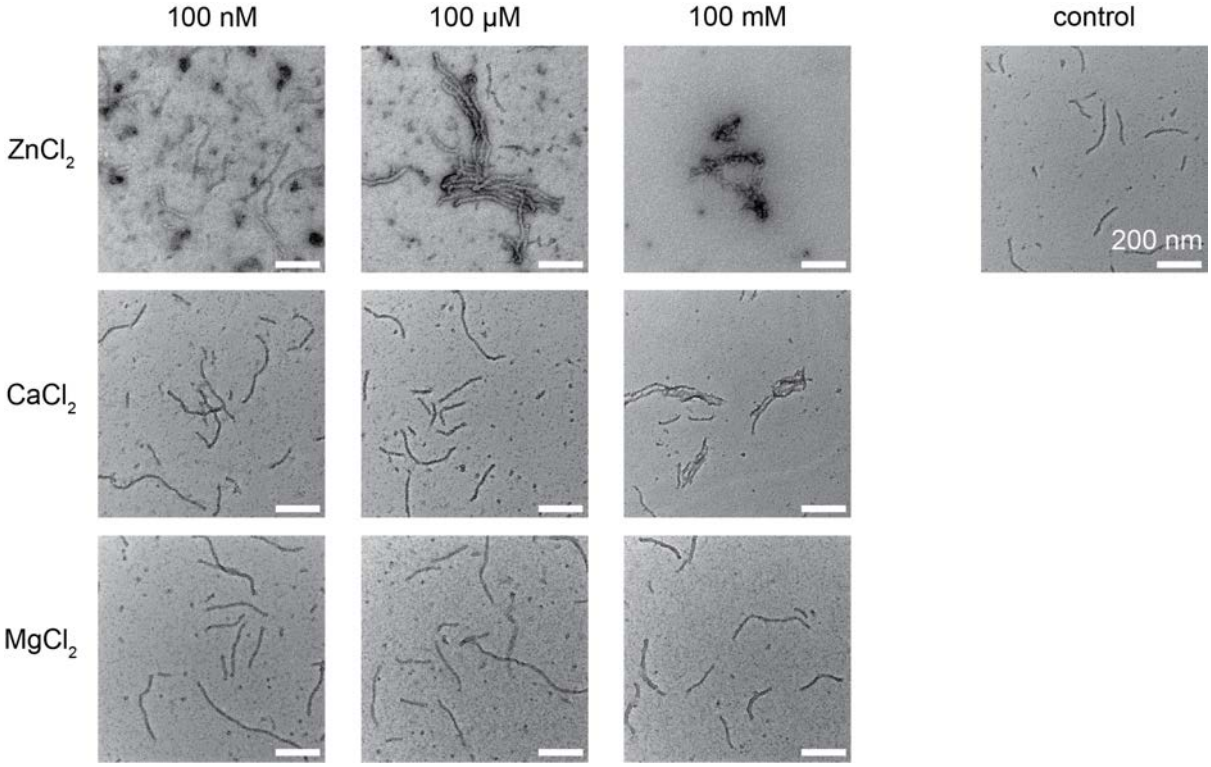

678

679 **Supplementary Figure 9: Effect of divalent cation salts on p62 filaments.** p62
680 filaments at 1 μM concentration were mixed with 100 nM, 100 μM and 100 mM of
681 $ZnCl_2$, $CaCl_2$ and $MgCl_2$, respectively. The samples were incubated for 30 minutes
682 and subsequently negatively stained. As a control, p62 filaments were mixed with
683 desalting buffer. For increasing concentrations of $ZnCl_2$from 100 μM and for $CaCl_2$
684 from 100 mM bundling of p62 filaments was observed. For $MgCl_2$ no clear effect of
685 bundling was observed.

686

References

Abramson, J., Adler, J., Dunger, J., Evans, R., Green, T., Pritzel, A., Ronneberger, O., Willmore, L., Ballard, A. J., Bambrick, J., Bodenstein, S. W., Evans, D. A., Hung, C.-C., O'Neill, M., Reiman, D., Tunyasuvunakool, K., Wu, Z., Žemgulytė, A., Arvaniti, E., … Jumper, J. M. (2024). Accurate structure prediction of biomolecular interactions with AlphaFold 3. *Nature*, *630*(8016), 493–500. https://doi.org/10.1038/s41586-024-07487-w

Beckers, M., & Sachse, C. (2020). Permutation testing of Fourier shell correlation for resolution estimation of cryo-EM maps. *Journal of Structural Biology*, *212*(1), 107579. https://doi.org/10.1016/j.jsb.2020.107579

Berkamp, S., Daviran, D., Smeets, M., Caignard, A., Jani, R. A., Sundermeyer, P., Jonker, C., Gerlach, S., Hoffmann, B., Lau, K., & Sachse, C. (2023). Correlative Light and Electron Cryo-Microscopy Workflow Combining Micropatterning, Ice Shield, and an In-Chamber Fluorescence Light Microscope. *Bio-Protocol*, *13*(24), e4901. https://doi.org/10.21769/bioprotoc.4901

Birgisdottir, Å. B., Lamark, T., & Johansen, T. (2013). The LIR motif – crucial for selective autophagy. *Journal of Cell Science*, *126*(15), 3237–3247. https://doi.org/10.1242/jcs.126128

Bjørkøy, G., Lamark, T., Brech, A., Outzen, H., Perander, M., Øvervatn, A., Stenmark, H., & Johansen, T. (2005). p62/SQSTM1 forms protein aggregates degraded by autophagy and has a protective effect on huntingtin-induced cell death. *The Journal of Cell Biology*, *171*(4), 603–614. https://doi.org/10.1083/jcb.200507002

Brangwynne, C. P., Eckmann, C. R., Courson, D. S., Rybarska, A., Hoege, C., Gharakhani, J., Jülicher, F., & Hyman, A. A. (2009). Germline P Granules Are Liquid Droplets That Localize by Controlled Dissolution/Condensation. *Science*, *324*(5935), 1729–1732. https://doi.org/10.1126/science.1172046

Buchholz, T. O., Krull, A., Shahidi, R., Pigino, G., Jékely, G., & Jug, F. (2019). Content-aware image restoration for electron microscopy. *Methods in Cell Biology*, *152*, 277–289. https://doi.org/10.1016/bs.mcb.2019.05.001

Chen, M., Ren, X., Nguyen, T. N., Khuu, G., Cook, A. S. I., Lazarou, M., & Hurley, J. H. (2023). *Structure and activation of the human autophagy-initiating ULK1C:PI3KC3-C1 supercomplex*. https://doi.org/10.1101/2023.06.01.543278

721 Christian, F., Krause, E., Houslay, M. D., & Baillie, G. S. (2014). PKA
722 phosphorylation of p62/SQSTM1 regulates PB1 domain interaction partner
723 binding. *Biochimica Et Biophysica Acta*, *1843*(11), 2765–2774.
724 https://doi.org/10.1016/j.bbamcr.2014.07.021

725 Ciani, B., Layfield, R., Cavey, J. R., Sheppard, P. W., & Searle, M. S. (2003).
726 Structure of the Ubiquitin-associated Domain of p62 (SQSTM1) and
727 Implications for Mutations That Cause Paget's Disease of Bone. *Journal of*
728 *Biological Chemistry*, *278*(39), 37409–37412.
729 https://doi.org/10.1074/jbc.m307416200

730 Ciuffa, R., Lamark, T., Tarafder, A. K., Guesdon, A., Rybina, S., Hagen, W.,
731 Johansen, T., & Sachse, C. (2015). The Selective Autophagy Receptor p62
732 Forms a Flexible Filamentous Helical Scaffold. *Cell Reports*, *11*(5), 748–758.
733 https://doi.org/10.1016/j.celrep.2015.03.062

734 Decuypere, J.-P., Kindt, D., Luyten, T., Welkenhuyzen, K., Missiaen, L., Smedt, H.
735 D., Bultynck, G., & Parys, J. B. (2013). mTOR-Controlled Autophagy Requires
736 Intracellular Ca2+ Signaling. *PLoS ONE*, *8*(4), e61020.
737 https://doi.org/10.1371/journal.pone.0061020

738 Desfosses, A., Ciuffa, R., Gutsche, I., & Sachse, C. (2014). SPRING – An image
739 processing package for single-particle based helical reconstruction from
740 electron cryomicrographs. *Journal of Structural Biology*, *185*(1), 15–26.
741 https://doi.org/10.1016/j.jsb.2013.11.003

742 Dupont, N., Chauhan, S., Arko-Mensah, J., Castillo, E. F., Masedunskas, A.,
743 Weigert, R., Robenek, H., Proikas-Cezanne, T., & Deretic, V. (2014). Neutral
744 Lipid Stores and Lipase PNPLA5 Contribute to Autophagosome Biogenesis.
745 *Current Biology*, *24*(6), 609–620. https://doi.org/10.1016/j.cub.2014.02.008

746 Duran, A., Amanchy, R., Linares, J. F., Joshi, J., Abu-Baker, S., Porollo, A., Hansen,
747 M., Moscat, J., & Diaz-Meco, M. T. (2011). p62 is a key regulator of nutrient
748 sensing in the mTORC1 pathway. *Molecular Cell*, *44*(1), 134–146.
749 https://doi.org/10.1016/j.molcel.2011.06.038

750 Feng, X., Sun, D., Li, Y., Zhang, J., Liu, S., Zhang, D., Zheng, J., Xi, Q., Liang, H.,
751 Zhao, W., Li, Y., Xu, M., He, J., Liu, T., Hasim, A., Ma, M., Xu, P., & Mi, N.
752 (2023). Local membrane source gathering by p62 body drives
753 autophagosome formation. *Nature Communications*, *14*(1), 7338.
754 https://doi.org/10.1038/s41467-023-42829-8

755 Feng, Y., He, D., Yao, Z., & Klionsky, D. J. (2014). The machinery of
756 macroautophagy. *Cell Research*, *24*(1), 24–41.
757 https://doi.org/10.1038/cr.2013.168

758 Ganeva, I., Lim, K., Boulanger, J., Hoffmann, P. C., Muriel, O., Borgeaud, A. C.,
759 Hagen, W. J. H., Savage, D. B., & Kukulski, W. (2023). The architecture of
760 Cidec-mediated interfaces between lipid droplets. *Cell Reports*, *42*(2),
761 112107. https://doi.org/10.1016/j.celrep.2023.112107

762 Ichimura, Y., Kumanomidou, T., Sou, Y., Mizushima, T., Ezaki, J., Ueno, T.,
763 Kominami, E., Yamane, T., Tanaka, K., & Komatsu, M. (2008). Structural
764 basis for sorting mechanism of p62 in selective autophagy. *The Journal of*
765 *Biological Chemistry*, *283*(33), 22847–22857.
766 https://doi.org/10.1074/jbc.M802182200

767 Ichimura, Y., Waguri, S., Sou, Y.-S., Kageyama, S., Hasegawa, J., Ishimura, R.,
768 Saito, T., Yang, Y., Kouno, T., Fukutomi, T., Hoshii, T., Hirao, A., Takagi, K.,
769 Mizushima, T., Motohashi, H., Lee, M.-S., Yoshimori, T., Tanaka, K.,
770 Yamamoto, M., & Komatsu, M. (2013). Phosphorylation of p62 activates the
771 Keap1-Nrf2 pathway during selective autophagy. *Molecular Cell*, *51*(5), 618–
772 631. https://doi.org/10.1016/j.molcel.2013.08.003

773 Itakura, E., & Mizushima, N. (2011). p62 targeting to the autophagosome formation
774 site requires self-oligomerization but not LC3 binding. *The Journal of Cell*
775 *Biology*, *192*(1), 17–27. https://doi.org/10.1083/jcb.201009067

776 Jakobi, A. J., Huber, S. T., Mortensen, S. A., Schultz, S. W., Palara, A., Kuhm, T.,
777 Shrestha, B. K., Lamark, T., Hagen, W. J. H., Wilmanns, M., Johansen, T.,
778 Brech, A., & Sachse, C. (2020). Structural basis of p62/SQSTM1 helical
779 filaments and their role in cellular cargo uptake. *Nature Communications*,
780 *11*(1), 440. https://doi.org/10.1038/s41467-020-14343-8

781 Joung, I., Strominger, J. L., & Shin, J. (1996). Molecular cloning of a
782 phosphotyrosine-independent ligand of the p56lck SH2 domain. *Proceedings*
783 *of the National Academy of Sciences*, *93*(12), 5991–5995.
784 https://doi.org/10.1073/pnas.93.12.5991

785 Kimanius, D., Dong, L., Sharov, G., Nakane, T., & Scheres, S. H. W. (2021). New
786 tools for automated cryo-EM single-particle analysis in RELION-4.0.
787 *Biochemical Journal*, *478*(24), 4169–4185.
788 https://doi.org/10.1042/BCJ20210708

789 Kirkin, V., Lamark, T., Sou, Y.-S., Bjørkøy, G., Nunn, J. L., Bruun, J.-A., Shvets, E.,
790 McEwan, D. G., Clausen, T. H., Wild, P., Bilusic, I., Theurillat, J.-P., Øvervatn,
791 A., Ishii, T., Elazar, Z., Komatsu, M., Dikic, I., & Johansen, T. (2009). A role
792 for NBR1 in autophagosomal degradation of ubiquitinated substrates.
793 *Molecular Cell*, *33*(4), 505–516. https://doi.org/10.1016/j.molcel.2009.01.020

794 Komatsu, M., Kurokawa, H., Waguri, S., Taguchi, K., Kobayashi, A., Ichimura, Y.,
795 Sou, Y.-S., Ueno, I., Sakamoto, A., Tong, K. I., Kim, M., Nishito, Y., Iemura,
796 S., Natsume, T., Ueno, T., Kominami, E., Motohashi, H., Tanaka, K., &
797 Yamamoto, M. (2010). The selective autophagy substrate p62 activates the
798 stress responsive transcription factor Nrf2 through inactivation of Keap1.
799 *Nature Cell Biology*, *12*(3), 213–223. https://doi.org/10.1038/ncb2021

800 Korfhage, J. L., Wan, N., Elhan, H., Kauffman, L., Pineda, M., Fuller, D. M., Thiam,
801 A. R., Reinisch, K. M., & Melia, T. J. (2023). *ATG2A-mediated bridge-like lipid*
802 *transport regulates lipid droplet accumulation*.
803 https://doi.org/10.1101/2023.08.14.553257

804 Kraft, L. J., Nguyen, T. A., Vogel, S. S., & Kenworthy, A. K. (2014). Size,
805 stoichiometry, and organization of soluble LC3-associated complexes.
806 *Autophagy*, *10*(5), 861–877. https://doi.org/10.4161/auto.28175

807 Kroemer, G., Mariño, G., & Levine, B. (2010). Autophagy and the Integrated Stress
808 Response. *Molecular Cell*, *40*(2), 280–293.
809 https://doi.org/10.1016/j.molcel.2010.09.023

810 Kumar, S., Rechav, K., Kaplan-Ashiri, I., & Gal, A. (2020). Imaging and quantifying
811 homeostatic levels of intracellular silicon in diatoms. *Science Advances*, *6*(42),
812 eaaz7554. https://doi.org/10.1126/sciadv.aaz7554

813 Kumsta, C., Chang, J. T., Lee, R., Tan, E. P., Yang, Y., Loureiro, R., Choy, E. H.,
814 Lim, S. H. Y., Saez, I., Springhorn, A., Hoppe, T., Vilchez, D., & Hansen, M.
815 (2019). The autophagy receptor p62/SQST-1 promotes proteostasis and
816 longevity in C. elegans by inducing autophagy. *Nature Communications*,
817 *10*(1), 5648. https://doi.org/10.1038/s41467-019-13540-4

818 Kwon, D. H., Park, O. H., Kim, L., Jung, Y. O., Park, Y., Jeong, H., Hyun, J., Kim, Y.
819 K., & Song, H. K. (2018). Insights into degradation mechanism of N-end rule
820 substrates by p62/SQSTM1 autophagy adapter. *Nature Communications*,
821 *9*(1), 3291. https://doi.org/10.1038/s41467-018-05825-x

822 Lamark, T., Perander, M., Outzen, H., Kristiansen, K., Øvervatn, A., Michaelsen, E.,
823 Bjørkøy, G., & Johansen, T. (2003). Interaction codes within the family of
824 mammalian Phox and Bem1p domain-containing proteins. *The Journal of*
825 *Biological Chemistry*, *278*(36), 34568–34581.
826 https://doi.org/10.1074/jbc.M303221200

827 Lamm, L., Righetto, R. D., Wietrzynski, W., Pöge, M., Martinez-Sanchez, A., Peng,
828 T., & Engel, B. D. (2022). MemBrain: A deep learning-aided pipeline for
829 detection of membrane proteins in Cryo-electron tomograms. *Computer*
830 *Methods and Programs in Biomedicine*, *224*, 106990.
831 https://doi.org/10.1016/j.cmpb.2022.106990

832 Lazarou, M., Sliter, D. A., Kane, L. A., Sarraf, S. A., Wang, C., Burman, J. L., Sideris,
833 D. P., Fogel, A. I., & Youle, R. J. (2015). The ubiquitin kinase PINK1 recruits
834 autophagy receptors to induce mitophagy. *Nature*, *524*(7565), 309–314.
835 https://doi.org/10.1038/nature14893

836 Lee, Y., Chou, T.-F., Pittman, S. K., Keith, A. L., Razani, B., & Weihl, C. C. (2017).
837 Keap1/Cullin3 Modulates p62/SQSTM1 Activity via UBA Domain
838 Ubiquitination. *Cell Reports*, *19*(1), 188–202.
839 https://doi.org/10.1016/j.celrep.2017.03.030

840 Lee, Y.-K., & Lee, J.-A. (2016). Role of the mammalian ATG8/LC3 family in
841 autophagy: differential and compensatory roles in the spatiotemporal
842 regulation of autophagy. *BMB Reports*, *49*(8), 424–430.
843 https://doi.org/10.5483/BMBRep.2016.49.8.081

844 Liu, Y.-T., Zhang, H., Wang, H., Tao, C.-L., Bi, G.-Q., & Zhou, Z. H. (2021). Isotropic
845 Reconstruction of Electron Tomograms with Deep Learning. *bioRxiv*,
846 2021.07.17.452128. https://doi.org/10.1101/2021.07.17.452128

847 MacVicar, T. D. B., Mannack, L. V. J. C., Lees, R. M., & Lane, J. D. (2015). Targeted
848 siRNA Screens Identify ER-to-Mitochondrial Calcium Exchange in Autophagy
849 and Mitophagy Responses in RPE1 Cells. *International Journal of Molecular*
850 *Sciences*, *16*(6), 13356–13380. https://doi.org/10.3390/ijms160613356

851 Mailler, E., Guardia, C. M., Bai, X., Jarnik, M., Williamson, C. D., Li, Y., Maio, N.,
852 Golden, A., & Bonifacino, J. S. (2021). The autophagy protein ATG9A enables
853 lipid mobilization from lipid droplets. *Nature Communications*, *12*(1), 6750.
854 https://doi.org/10.1038/s41467-021-26999-x

855 Man, N., Chen, Y., Zheng, F., Zhou, W., & Wen, L.-P. (2010). Induction of genuine
856 autophagy by cationic lipids in mammalian cells. *Autophagy*, *6*(4), 449–454.
857 https://doi.org/10.4161/auto.6.4.11612

858 Mastronarde, D. N. (2005). Automated electron microscope tomography using robust
859 prediction of specimen movements. *Journal of Structural Biology*, *152*(1), 36–
860 51. https://doi.org/10.1016/j.jsb.2005.07.007

861 Mastronarde, D. N., & Held, S. R. (2017). Automated tilt series alignment and
862 tomographic reconstruction in IMOD. *Journal of Structural Biology*, *197*(2),
863 102–113. https://doi.org/10.1016/j.jsb.2016.07.011

864 Mizushima, N., Yamamoto, A., Hatano, M., Kobayashi, Y., Kabeya, Y., Suzuki, K.,
865 Tokuhisa, T., Ohsumi, Y., & Yoshimori, T. (2001). Dissection of
866 Autophagosome Formation Using Apg5-Deficient Mouse Embryonic Stem
867 Cells. *The Journal of Cell Biology*, *152*(4), 657–668.
868 https://doi.org/10.1083/jcb.152.4.657

869 Mizushima, N., Yoshimori, T., & Ohsumi, Y. (2011). The Role of Atg Proteins in
870 Autophagosome Formation. *Annual Review of Cell and Developmental*
871 *Biology*, *27*(1), 107–132. https://doi.org/10.1146/annurev-cellbio-092910-
872 154005

873 Mo, R. H., Zaro, J. L., Ou, J.-H. J., & Shen, W.-C. (2012). Effects of Lipofectamine
874 2000/siRNA Complexes on Autophagy in Hepatoma Cells. *Molecular*
875 *Biotechnology*, *51*(1), 1–8. https://doi.org/10.1007/s12033-011-9422-6

876 Morin, A., Eisenbraun, B., Key, J., Sanschagrin, P. C., Timony, M. A., Ottaviano, M.,
877 & Sliz, P. (2013). Cutting Edge: Collaboration gets the most out of software.
878 *eLife*, *2*, e01456. https://doi.org/10.7554/eLife.01456

879 Morishita, H., Eguchi, S., Kimura, H., Sasaki, J., Sakamaki, Y., Robinson, M. L.,
880 Sasaki, T., & Mizushima, N. (2013). Deletion of Autophagy-related 5 (Atg5)
881 and Pik3c3 Genes in the Lens Causes Cataract Independent of Programmed
882 Organelle Degradation. *Journal of Biological Chemistry*, *288*(16), 11436–
883 11447. https://doi.org/10.1074/jbc.M112.437103

884 Nakatogawa, H., Suzuki, K., Kamada, Y., & Ohsumi, Y. (2009). Dynamics and
885 diversity in autophagy mechanisms: lessons from yeast. *Nature Reviews*
886 *Molecular Cell Biology*, *10*(7), 458–467. https://doi.org/10.1038/nrm2708

887 Omrane, M., M'Barek, K. B., Santinho, A., Nguyen, N., Nag, S., Melia, T. J., &
888 Thiam, A. R. (2023). LC3B is lipidated to large lipid droplets during prolonged
889 starvation for noncanonical autophagy. *Developmental Cell*, *58*(14), 1266–
890 1281.e7. https://doi.org/10.1016/j.devcel.2023.05.009

891 Otomo, C., Metlagel, Z., Takaesu, G., & Otomo, T. (2013). Structure of the human
892 ATG12 conjugate required for LC3 lipidation in autophagy. *Nature Structural &*
893 *Molecular Biology*, *20*(1), 59–66. https://doi.org/10.1038/nsmb.2431

894 Pankiv, S., Clausen, T., Lamark, T., Brech, A., Bruun, J.-A., Outzen, H., Øvervatn,
895 A., Bjørkøy, G., & Johansen, T. (2007). p62/SQSTM1 Binds Directly to
896 Atg8/LC3 to Facilitate Degradation of Ubiquitinated Protein Aggregates by
897 Autophagy. *Journal of Biological Chemistry*, *282*(33), 24131–24145.
898 https://doi.org/10.1074/jbc.m702824200

899 Pettersen, E. F., Goddard, T. D., Huang, C. C., Couch, G. S., Greenblatt, D. M.,
900 Meng, E. C., & Ferrin, T. E. (2004). UCSF Chimera—A visualization system
901 for exploratory research and analysis. *Journal of Computational Chemistry*,
902 *25*(13), 1605–1612. https://doi.org/10.1002/jcc.20084

903 Puissant, A., Fenouille, N., & Auberger, P. (2012). When autophagy meets cancer
904 through P62/SQSTM1. *American Journal of Cancer Research*, *2*(4), 397–413.

905 Puri, C., Renna, M., Bento, Carla F., Moreau, K., & Rubinsztein, David C. (2013).
906 Diverse Autophagosome Membrane Sources Coalesce in Recycling
907 Endosomes. *Cell*, *154*(6), 1285–1299.
908 https://doi.org/10.1016/j.cell.2013.08.044

909 Robichaud, S., Fairman, G., Vijithakumar, V., Mak, E., Cook, D. P., Pelletier, A. R.,
910 Huard, S., Vanderhyden, B. C., Figeys, D., Lavallée-Adam, M., Baetz, K., &
911 Ouimet, M. (2021). Identification of novel lipid droplet factors that regulate
912 lipophagy and cholesterol efflux in macrophage foam cells. *Autophagy*,
913 *17*(11), 3671–3689. https://doi.org/10.1080/15548627.2021.1886839

914 Rogov, V., Dötsch, V., Johansen, T., & Kirkin, V. (2014). Interactions between
915 Autophagy Receptors and Ubiquitin-like Proteins Form the Molecular Basis for
916 Selective Autophagy. *Molecular Cell*, *53*(2), 167–178.
917 https://doi.org/10.1016/j.molcel.2013.12.014

918 Rohou, A., & Grigorieff, N. (2015). CTFFIND4: Fast and accurate defocus estimation
919 from electron micrographs. *Journal of Structural Biology*, *192*(2), 216–221.
920 https://doi.org/10.1016/j.jsb.2015.08.008

921 Rosenthal, P. B., & Henderson, R. (2003). Optimal Determination of Particle
922 Orientation, Absolute Hand, and Contrast Loss in Single-particle Electron
923 Cryomicroscopy. *Journal of Molecular Biology*, *333*(4), 721–745.
924 https://doi.org/10.1016/j.jmb.2003.07.013

925 Scheres, S. H. W. (2012). RELION: Implementation of a Bayesian approach to cryo-
926 EM structure determination. *Journal of Structural Biology*, *180*(3), 519–530.
927 https://doi.org/https://doi.org/10.1016/j.jsb.2012.09.006

928 Schindelin, J., Arganda-Carreras, I., Frise, E., Kaynig, V., Longair, M., Pietzsch, T.,
929 Preibisch, S., Rueden, C., Saalfeld, S., Schmid, B., Tinevez, J.-Y., White, D.
930 J., Hartenstein, V., Eliceiri, K., Tomancak, P., & Cardona, A. (2012). Fiji: an
931 open-source platform for biological-image analysis. *Nature Methods*, *9*(7),
932 676. https://doi.org/10.1038/nmeth.2019

933 Schott, M. B., Weller, S. G., Schulze, R. J., Krueger, E. W., Drizyte-Miller, K., Casey,
934 C. A., & McNiven, M. A. (2019). Lipid droplet size directs lipolysis and
935 lipophagy catabolism in hepatocytes. *Journal of Cell Biology*, *218*(10), 3320–
936 3335. https://doi.org/10.1083/jcb.201803153

937 Shpilka, T., Weidberg, H., Pietrokovski, S., & Elazar, Z. (2011). Atg8: an autophagy-
938 related ubiquitin-like protein family. *Genome Biology*, *12*(7), 226.
939 https://doi.org/10.1186/gb-2011-12-7-226

940 Shpilka, T., Welter, E., Borovsky, N., Amar, N., Mari, M., Reggiori, F., & Elazar, Z.
941 (2015). Lipid droplets and their component triglycerides and steryl esters
942 regulate autophagosome biogenesis. *The EMBO Journal*, *34*(16), 2117–2131.
943 https://doi.org/10.15252/embj.201490315

944 Singh, R., Kaushik, S., Wang, Y., Xiang, Y., Novak, I., Komatsu, M., Tanaka, K.,
945 Cuervo, A. M., & Czaja, M. J. (2009). Autophagy regulates lipid metabolism.
946 *Nature*, *458*(7242), 1131–1135. https://doi.org/10.1038/nature07976

947 Smeets, M., Bieber, A., Capitanio, C., Schioetz, O., van der Heijden, T., Effting, A.,
948 Piel, É., Lazem, B., Erdmann, P., & Plitzko, J. (2021). Integrated Cryo-
949 Correlative Microscopy for Targeted Structural Investigation In Situ.
950 *Microscopy Today*, *29*(6), 20–25.
951 https://doi.org/10.1017/S1551929521001280

952 Stirling, D. R., Swain-Bowden, M. J., Lucas, A. M., Carpenter, A. E., Cimini, B. A., &
953 Goodman, A. (2021). CellProfiler 4: improvements in speed, utility and

usability. *BMC Bioinformatics*, *22*(1), 433. https://doi.org/10.1186/s12859-021-04344-9

Sun, D., Wu, R., Li, P., & Yu, L. (2019). Phase Separation in Regulation of Aggrephagy. *Journal of Molecular Biology*, *432*(1), 160–169. https://doi.org/10.1016/j.jmb.2019.06.026

Sun, D., Wu, R., Zheng, J., Li, P., & Yu, L. (2018). Polyubiquitin chain-induced p62 phase separation drives autophagic cargo segregation. *Cell Research*, *28*(4), 405–415. https://doi.org/10.1038/s41422-018-0017-7

Tegunov, D., & Cramer, P. (2019). Real-time cryo-electron microscopy data preprocessing with Warp. *Nature Methods*, *16*(11), 1146–1152. https://doi.org/10.1038/s41592-019-0580-y

Thörnig, P. (2021). JURECA: Data Centric and Booster Modules implementing the Modular Supercomputing Architecture at Jülich Supercomputing Centre. *Journal of Large-Scale Research Facilities*, *7*. https://doi.org/https://doi.org/10.17815/jlsrf-7-182

Toro-Nahuelpan, M., Zagoriy, I., Senger, F., Blanchoin, L., Théry, M., & Mahamid, J. (2019). Tailoring cryo-electron microscopy grids by photo-micropatterning for in-cell structural studies. *bioRxiv*, 676189. https://doi.org/10.1101/676189

Tsai, T.-H., Chen, E., Li, L., Saha, P., Lee, H.-J., Huang, L.-S., Shelness, G. S., Chan, L., & Chang, B. H.-J. (2017). The constitutive lipid droplet protein PLIN2 regulates autophagy in liver. *Autophagy*, *13*(7), 1130–1144. https://doi.org/10.1080/15548627.2017.1319544

Turco, E., Savova, A., Gere, F., Ferrari, L., Romanov, J., Schuschnig, M., & Martens, S. (2021). Reconstitution defines the roles of p62, NBR1 and TAX1BP1 in ubiquitin condensate formation and autophagy initiation. *Nature Communications*, *12*(1), 5212. https://doi.org/10.1038/s41467-021-25572-w

Turco, E., Witt, M., Abert, C., Bock-Bierbaum, T., Su, M.-Y., Trapannone, R., Sztacho, M., Danieli, A., Shi, X., Zaffagnini, G., Gamper, A., Schuschnig, M., Fracchiolla, D., Bernklau, D., Romanov, J., Hartl, M., Hurley, J. H., Daumke, O., & Martens, S. (2019). FIP200 Claw Domain Binding to p62 Promotes Autophagosome Formation at Ubiquitin Condensates. *Molecular Cell*, *74*(Acta Crystallogr. D Biol. Crystallogr. 66 2010), 330–346.e11. https://doi.org/10.1016/j.molcel.2019.01.035

Wagner, T., Merino, F., Stabrin, M., Moriya, T., Antoni, C., Apelbaum, A., Hagel, P., Sitsel, O., Raisch, T., Prumbaum, D., Quentin, D., Roderer, D., Tacke, S., Siebolds, B., Schubert, E., Shaikh, T. R., Lill, P., Gatsogiannis, C., & Raunser, S. (2019). SPHIRE-crYOLO is a fast and accurate fully automated particle picker for cryo-EM. *Communications Biology*, *2*(1), 218. https://doi.org/10.1038/s42003-019-0437-z

Wang, L., Zhou, J., Yan, S., Lei, G., Lee, C.-H., & Yin, X.-M. (2017). Ethanol-triggered Lipophagy Requires SQSTM1 in AML12 Hepatic Cells. *Scientific Reports*, *7*(1), 12307. https://doi.org/10.1038/s41598-017-12485-2

Wang, Y., Dahmane, S., Ti, R., Mai, X., Zhu, L., Carlson, L.-A., & Stjepanovic, G. (2024). Structural basis for lipid transfer by the ATG2A–ATG9A complex. *Nature Structural & Molecular Biology*. https://doi.org/10.1038/s41594-024-01376-6

Watson, J. D., & Crick, F. H. (1953). Molecular structure of nucleic acids; a structure for deoxyribose nucleic acid. *Nature*, *171*(4356), 737–738. https://doi.org/10.1038/171737a0

Wen, X., & Klionsky, D. J. (2016). An overview of macroautophagy in yeast. *Journal of Molecular Biology*, *428*(9), 1681–1699. https://doi.org/10.1016/j.jmb.2016.02.021

Wolf, S. G., Mutsafi, Y., Dadosh, T., Ilani, T., Lansky, Z., Horowitz, B., Rubin, S., Elbaum, M., & Fass, D. (2017). 3D visualization of mitochondrial solid-phase calcium stores in whole cells. *eLife*, *6*, e29929. https://doi.org/10.7554/elife.29929

WOLF, S. G., REZ, P., & ELBAUM, M. (2015). Phosphorus detection in vitrified bacteria by cryo-STEM annular dark-field analysis. *Journal of Microscopy*, *260*(2), 227–233. https://doi.org/10.1111/jmi.12289

Xie, Z., & Klionsky, D. J. (2007). Autophagosome formation: core machinery and adaptations. *Nature Cell Biology*, *9*(10), 1102–1109. https://doi.org/10.1038/ncb1007-1102

Yamamoto, H., Kakuta, S., Watanabe, T. M., Kitamura, A., Sekito, T., Kondo-Kakuta, C., Ichikawa, R., Kinjo, M., & Ohsumi, Y. (2012). Atg9 vesicles are an important membrane source during early steps of autophagosome formation. *Journal of Cell Biology*, *198*(2), 219–233. https://doi.org/10.1083/jcb.201202061

1021 Yan, Y., Wang, H., Wei, C., Xiang, Y., Liang, X., Phang, C.-W., & Jiao, R. (2019).
1022 HDAC6 regulates lipid droplet turnover in response to nutrient deprivation via
1023 p62-mediated selective autophagy. *Journal of Genetics and Genomics*, *46*(4),
1024 221–229. https://doi.org/10.1016/j.jgg.2019.03.008

1025 Yao, W., Chen, Y., Zhang, Y., Zhong, S., Ye, M., Chen, Y., Fan, S., Ye, M., Yang,
1026 H., Li, Y., Wu, C., Fan, M., Feng, S., He, Z., Zhou, L., Zhang, L., Wang, Y.,
1027 Liu, W., Tong, J., … Yi, C. (2024). Ca2+-triggered Atg11-Bmh1/2-Snf1
1028 complex assembly initiates autophagy upon glucose starvation. *The Journal*
1029 *of Cell Biology*, *223*(9), e202310049. https://doi.org/10.1083/jcb.202310049

1030 Zaffagnini, G., Savova, A., Danieli, A., Romanov, J., Tremel, S., Ebner, M.,
1031 Peterbauer, T., Sztacho, M., Trapannone, R., Tarafder, A. K., Sachse, C., &
1032 Martens, S. (2018a). P62 filaments capture and present ubiquitinated cargos
1033 for autophagy. *The EMBO Journal*, *37*(5), e98308.
1034 https://doi.org/10.15252/embj.201798308

1035 Zaffagnini, G., Savova, A., Danieli, A., Romanov, J., Tremel, S., Ebner, M.,
1036 Peterbauer, T., Sztacho, M., Trapannone, R., Tarafder, A. K., Sachse, C., &
1037 Martens, S. (2018b). Phasing out the bad-How SQSTM1/p62 sequesters
1038 ubiquitinated proteins for degradation by autophagy. *Autophagy*, *14*(7), 1280–
1039 1282. https://doi.org/10.1080/15548627.2018.1462079

1040 Zhang, J., Tripathi, D. N., Jing, J., Alexander, A., Kim, J., Powell, R. T., Dere, R.,
1041 Tait-Mulder, J., Lee, J.-H., Paull, T. T., Pandita, R. K., Charaka, V. K.,
1042 Pandita, T. K., Kastan, M. B., & Walker, C. L. (2015). ATM functions at the
1043 peroxisome to induce pexophagy in response to ROS. *Nature Cell Biology*,
1044 *17*(10), 1259–1269. https://doi.org/10.1038/ncb3230

1045 Zheng, Q., Chen, Y., Chen, D., Zhao, H., Feng, Y., Meng, Q., Zhao, Y., & Zhang, H.
1046 (2022). Calcium transients on the ER surface trigger liquid-liquid phase
1047 separation of FIP200 to specify autophagosome initiation sites. *Cell*.
1048 https://doi.org/10.1016/j.cell.2022.09.001

1049 Zheng, S., Wolff, G., Greenan, G., Chen, Z., Faas, F. G. A., Bárcena, M., Koster, A.
1050 J., Cheng, Y., & Agard, D. A. (2022). AreTomo: An integrated software
1051 package for automated marker-free, motion-corrected cryo-electron
1052 tomographic alignment and reconstruction. *Journal of Structural Biology: X*, *6*,
1053 100068. https://doi.org/10.1016/j.yjsbx.2022.100068

Zierold, K., Schäfer, D., & Pietruschka, F. (1984). The element distribution in ultrathin cryosections of cultivated fibroblast cells. *Histochemistry*, *80*(4), 333–337. https://doi.org/10.1007/bf00495413

1058 # Materials & Methods

1059 **Protein expression, purification of p62, 4x-linear-ubiquitin and**
1060 **LC3B**

1061 Full-length p62 (440 residues) was cloned into a pETM43 expression vector
1062 containing an N-terminal maltose-binding-protein (MBP) tag and a C-terminal His-
1063 tag. Both tags featured a recognition sequence for HRV-3C protease, facilitating their
1064 removal after purification. 4x-linear-Ubiquitin, CFP-LC3B, and LC3B with an
1065 additional C-terminal cysteine residue were cloned into pGEX expression vector
1066 containing an N-terminal Glutathione-S-Transferase (GST) tag with HRV-3C
1067 protease cleavage site. For protein expression E. *coli* BL21 (DE3) cells were used,
1068 with bacterial cultures grown at 37°C in Terrific Broth (TB) medium to an OD_{600} of ~2.
1069 Induction with IsoPropylThioGalactoside (IPTG) followed and cells were left to grow
1070 overnight at 23°C. Cells were harvested and the pellet was stored at -80 °C until
1071 further use.

1072 After thawing on ice, cells were resuspended in lysis buffer [50 mM HEPES, pH 8.0,
1073 300 mM NaCl, 2.5 mM $MgSO_4$, 10 µM $ZnCl_2$, 0.5 mM TCEP and 1 tablet EDTA-free
1074 protease inhibitor cocktail] and lysed using a cell disruptor at 1.85 bar. Cell debris
1075 was removed by centrifugation and the cleared lysate was applied to a Ni-NTA
1076 affinity column. The column was washed twice with lysis buffer containing 10 mM
1077 and 20 mM imidazole, respectively, and protein was eluted with lysis buffer
1078 containing 300 mM imidazole. Eluted protein fractions were pooled and subsequently
1079 applied to an amylose resin that binds MBP-fusion proteins with high affinity. The
1080 column was washed with lysis buffer and the protein was eluted with lysis buffer
1081 containing 25 mM maltose. Eluted protein fractions were pooled, and buffer was
1082 exchanged to desalting buffer [50 mM HEPES, pH 8.0, 300 mM NaCl and 0.5 mM
1083 TCEP] using Zeba desalting columns.

1084 For the purification of LC3b and GST-4xUb, the cell pellets were resuspended in
1085 lysis buffer [50 mM HEPES, pH 7.4, 300 mM NaCl, 1 mM DTT, and 1 tablet EDTA-
1086 free protease inhibitor cocktail] and lysed using a cell disruptor at 1.9 bar. The
1087 cleared lysate was applied to Glutathione Sepharose 4 Fast Flow GST-tagged
1088 protein purification resin (Cytiva, Cat No 17513201), washed with 10 column volume
1089 lysis buffer, and eluted in lysis buffer containing 10 mM reduced glutathione. Elution
1090 fractions containing the protein of interested were pooled, further purified by size
1091 exclusion chromatography via SD200 16/600 column (Cytiva) [in 50 mM HEPES, pH
1092 7.4, 150 mM NaCl, 1 mM DTT], and frozen at -80°C for storage.

p62 filament formation and labeling

Protein was concentrated to approximately 2 mg/mL using a 30 kDa Amicon concentrator and subsequently incubated with 1:2.5 mass ratio of GST-HRV-3C protease for 3 h at room temperature and overnight at 4°C to remove the MBP and His-tag, allowing p62 filament formation. Filaments were isolated by centrifugation at 20,000 x g for 30 min and resuspended in desalting buffer. Isolated filaments were labeled to lysine residues by incubating with 1:1 molar ratio of Cy5-NHS for 1 h at room temperature and overnight at 4°C. Excess dye was removed by centrifugation, labeled filaments were resuspended in storage buffer [50 mM HEPES, pH 8.0, 50 mM NaCl and 0.5 mM TCEP] and stored at 4°C until further use.

Cryo-EM structure determination of p62 filaments

Quantifoil Cu 200 mesh R1.2/R1.3 were glow discharged, and 2-5µL of the protein sample was applied in a Vitrobot mark IV (ThermoFischer Scientific). The sample chamber was maintained at 70-100 % humidity and 4-10 °C, with a 2-6 s blotting time before plunging into ethane/propane mixture. Data collection was performed using SerialEM(Mastronarde, 2005) on a Talos Arctica 200 KeV G2 transmission electron microscope (ThermoFischer Scientific), equipped with a K3 direct electron detector camera and Quantum GIF filter (Gatan, Inc). Approximately 4000 micrographs were collected in counted superresolution mode at 100,000x magnification with an underfocus range of -0.5 µm to -3 µm. The micrographs were motion corrected in WARP(Tegunov & Cramer, 2019) and particles were picked using the deep-learning based object detection software crYOLO (Wagner et al., 2019). The picked particle locations and micrographs were imported into RELION(Scheres, 2012) that used CTFFIND4 for CTF estimation(Rohou & Grigorieff, 2015). Next, particle locations were extracted with a 90 % overlap yielding approximately 5,000,000 segments of a box size of 352 Å. Two rounds of 2D classification were performed in order to remove heterogeneous particles. Classes with clearly defined PB1 domains were then selected, leading to a total of 1,600,000 segments. The helical parameters as determined by Jakobi et al. (Jakobi et al., 2020) of truncated p62 helical filaments were taken as starting conditions in a supervised 3D classification in RELION. Two of the 13.7 nm pitch classes were chosen yielding 158,000 segments and subjected to 3D auto-refinement in RELION, where the symmetry parameters converged. The final resolution was estimated by FSC using the 0.143 cutoff(Rosenthal & Henderson, 2003) and FDR-FSC criterion(Beckers & Sachse, 2020). Maps were rendered in UCSF Chimera (Pettersen et al., 2004).

1129 ## Single-particle fluorescence imaging in TIRF mode

1130 Surface imaging was performed with an inverted microscope (Olympus IX-81,
1131 Olympus Corp., Shinjuku, Japan) in total internal reflection fluorescence (TIRF)
1132 mode. Molecules were excited using lasers at 488 and 639 nm (Sapphire 488-200
1133 and Obis 637-140, Coherent Inc.) focused off-axis into the back-focal plane of an oil-
1134 immersion objective (Olympus UApoN, 100x, NA=1.49, Olympus Corp). The
1135 excitation power and corresponding intensity at the sample stage were 3.25 mW and
1136 10.2 W/cm^2 for the blue laser, and 2.2 mW and 6.8 W/cm^2 for the red laser. The
1137 imaging was performed on an EMCCD camera (Andor iXon Ultra 888, Andor
1138 Technology) with 50, 100, 40 and 100 ms exposure time for Supplementary Videos
1139 1-4, corresponding to 20, 10, 25 and 10 fps. Midway through acquiring
1140 Supplementary Video 2, the illumination was switched from blue to red laser to
1141 observe the same p62 filament with LC3b bound to it. Each video consists of 200
1142 frames. Image analysis and video processing were carried out using Fiji (ImageJ,
1143 version 2.14.0) (Schindelin et al., 2012). The emitted fluorescence was collected with
1144 the same objective (objective based TIRF) and passed through a dual-band dichroic
1145 mirror as well as a dual-band emission filter (ZT488/640rpc and ZET488/640m,
1146 Chroma Technology Corp). p62 filaments-Cy5 and CFP-LC3b were diluted to
1147 concentrations of a few nM, and mixed in a 1:1 molar ratio. GST-4xUb was added at
1148 a concentration of 5 μM.

1149 ## Negative staining electron microscopy

1150 For negative staining, 3.5 μL of the sample was applied onto glow-discharged
1151 carbon-formvar-coated 300-mesh copper grids and allowed to absorb for 2 min
1152 before blotted according to the side-blotting method. The sample was subsequently
1153 stained for 30 s with 6 μL 2% uranyl acetate, blotted and allowed to dry. Negatively
1154 stained samples were examined on a Talos L120C G2 transmission electron
1155 microscope (ThermoFisher Scientific), operated at 120 kV. Micrographs at high
1156 magnification (45,000x and 92,000x) were collected on a 4k x 4k Ceta 16M CEMOS
1157 camera using TEM Imaging & Analysis Software (TIA, ThermoFisher Scientific).

1158 ## Cryo-electron tomography of reconstituted p62 filaments

1159 p62 filament cryo-EM grids were prepared as described above. Tilt series were
1160 recorded on a 200 kV Talos Arctica G2 transmission electron microscope
1161 (ThermoFisher Scientific), equipped with a Bioquantum GIF (Gatan, Inc) a Volta
1162 Phase Plate and a K3 direct electron detector (Gatan, Inc) using SerialEM
1163 (Mastronarde, 2005). Each tilt was recorded as movie at 63.000x magnification with

1164 a 0.681 Å/pixel size in super resolution mode and a dose of approximately 2.0
1165 e/Å^2/tilt, 10 frames per tilt, and a total dose per tilt series of approximately 130 e/Å^2.
1166 All tilt series were recorded from -54° to 54° with 3° increments, using a dose-
1167 symmetric bidirectional acquisition scheme and a nominal defocus of -1.2 µm. The
1168 raw data was motion corrected and CTF corrected using WARP (version
1169 1.0.9)(Tegunov & Cramer, 2019) and the tilt series were reconstructed using
1170 IMOD(Mastronarde & Held, 2017).

1171 GST-4x-linear-Ubiquitin and p62 filaments were prepared as described above. 15
1172 μM of GST-4x-linear-Ubiquitin were mixed with 1 μM p62 filaments. After 4 minutes
1173 incubation time at 4°C, the formed phase separation droplets were negatively
1174 stained as described above or plunge frozen with a Vitrobot Mark IV (ThermoFisher
1175 Scientific). 50 nm SUVs were prepared containing 5% DSPE-PEG(2000) maleimide
1176 (Avanti Polar lipids, Cat No 880126) in DOPS (Avantiv Polar lipids, Cat No 840035).
1177 The liposomes were incubated with 100 μM LC3b-Cys for 16 h at 4°C before
1178 removing unbound LC3b-Cys by size exclusion chromatography on Sepharcyl S-500
1179 at Äkta Micro (Cytiva). A total of 2 mg/ml of liposomes were mixed with 1 μM p62
1180 filaments and incubated for 5 min at 4 °C. The sample was plunge frozen at a Leica
1181 GM2 plunge freezer (Leica). Tomograms were collected at a Titan Krios 300 keV
1182 TEM equipped with an BioContinuum energy filter and K3 camera at 64,000x using
1183 Tomo5 software (ThermoFisher Scientific). The tilt series were recorded from -60° to
1184 60° with a 3° increment in a dose-symmetric bidirectional acquisition scheme. An
1185 electron dose of 4.0 e$^-$/Å^2/tilt with 6 frames per tilt, resulted in a total dose per tilt
1186 series of approximately 160 e$^-$/Å^2. The defocus was varied between -2.0 to -4.0 µm.
1187 The images were motion corrected in WARP (Tegunov & Cramer, 2019) and
1188 tomograms reconstructed with AreTomo (S. Zheng et al., 2022). Overall binning was
1189 16x and resulted in a pixel size of 11.2 Å. Tomograms were denoised and missing
1190 wedge corrected with IsoNet (Liu et al., 2021).

1191 Cell culture and transfection

1192 Cell culture experiments were carried out in human RPE1 cells (hTERT RPE1, CRL-
1193 4000, ATCC) cultured at 37°C and 5% CO_2 in DMEM GlutaMAX media (Gibco, Cat
1194 No 31331028) supplemented with 10% FCS (Sigma-Aldrich, Cat No F7524) and
1195 Pen/Strep (Gibco, Cat No 15140122). For confocal microscopy experiments prior to
1196 plunge-freezing, the culturing media was substituted with media of low fluorescence
1197 background; Fluorobrite DMEM (Gibco, Cat No A1896701). Additional experiments
1198 were performed on RPE1 cells stably expressing human mCherry-p62. Transient
1199 expression of mCherry-p62 was executed by transfection with FugeneHD (Promega,

1200 Cat No E2311) and a modified pDEST vector containing the human wildtype p62
1201 gene fused with an N-terminal mCherry sequence (Pankiv et al., 2007). Knockdown
1202 experiments were carried out by transfection with RNAiMAX (ThermoFisher, Cat No
1203 13778075) and ON-TARGETplus SMARTpool siRNA against ATG5 (Dharmcon
1204 Horizon Discovery, Cat No L-004374-00-0005), GADPH (Dharmcon Horizon
1205 Discovery, Cat No D-001830-10-05) and a non-targeting control (Dharmcon Horizon
1206 Discovery, Cat No D-001810-10-05). Follow-up experiments were performed 72
1207 hours after a reverse transfection with 75 nm siRNA. Lipid droplets were stained with
1208 1:500 Lipi-Blue (Dojindo, Cat No LD01-10) for 24 hours. Lysosomes were stained
1209 with the CytoPainter Lysosomal staining kit (Abcam, Cat No ab112136).

1210 Western Blot

1211 Cells were lysed by a quick wash with ice cold PBS (Gibco, Cat No 10010056) and a
1212 subsequent 15 min incubation in ice cold RIPA buffer (Sigma-Aldrich, Cat No R0278-
1213 50mL) supplemented with a protease inhibitor cocktail (Roche, Cat No
1214 11836170001). Cell lysate was collected with a cell scraper before removing the cell
1215 debris by centrifugation. Total protein content was quantified and corrected using a
1216 Pierce 660 nm assay (ThermoFisher, Cat No 22662) before boiling the sampling in a
1217 reducing sample buffer and separation on a 4-15 % mini-PROTEAN Precast SDS-
1218 PAGE (Bio-Rad, Cat No 4561085). Transfer to PVDF membrane was performed
1219 using a Trans-Blot pack (Bio-Rad, Cat No 1704156) and the membrane was blocked
1220 for 2 h in 2 % BSA in TBST at 4 °C. The membrane was incubated overnight with
1221 primary antibody in 1 % BSA in TBST at 4 °C, washed 3 times in TBST before the
1222 secondary antibody was added for 2 h in 1 % BSA in TBST at 4 °C. Prior to imaging
1223 on the Azure Sapphire RGB Biomolecular Imager (Azure Biosystems), the
1224 membrane was washed 3 times in TBST and incubated in Azure Radiance Q HRP
1225 (Biozym, Cat No 512101). The following antibodies were used: polyclonal rabbit anti-
1226 p62 (MBL International, Cat No PM045), monoclonal rabbit anti-ATG5 (Abcam, Cat
1227 No ab108327), monoclonal mouse anti-GADPH (Invitrogen, Cat No MA1-16757),
1228 polyclonal rabbit anti-LC3 (Abcam, Cat No ab48394), goat anti-mouse HRP
1229 conjugate (ThermoFisher Cat No 32230), and goat anti-rabbit HRP conjugate
1230 (ThermoFisher, Cat No 31460). Band intensity quantifications were performed using
1231 ImageLab (BioRad, version 6.1.0).

1232 Cellular tomography grid preparation

1233 RPE1 Cells were seeded on micropatterned grids before plunge freezing, For a more
1234 detailed protocol see Berkamp et al. Bio-Protocols 2023 (Berkamp et al., 2023; Toro-

1235 Nahuelpan et al., 2019). Briefly, 200 mesh gold Quantifoil R2/1 grids with a SiO_2
1236 support layer (Quantifoil, Cat No N1-S15nAu20-01) were glow discharged and
1237 treated with PLL-g-PEG (SuSoS, PLL(20)-g[3.5]- PEG(5)) overnight. Next, the grids
1238 were washed in PBS and placed in drops of 14.5 mg/mL PLPP (Alvéole, Cat No
1239 PLPP) and 20 µm circles in the center of 10x10 grid squares were micropatterned
1240 with a PRIMO photopatterning device (Alvéole, Photopatterning Device consisting of
1241 a DMD + laser 375 nm, 75 mW module, and driving electronics). The grids were then
1242 washed thoroughly in PBS and incubated in human fibronectin immediately before
1243 use (Gibco, Cat No PHE0023). The cells were trypsinized (Gibco, Cat No
1244 25300054), passed through a 40 µm cell strainer (PluriSelect, Cat No 43-10040-40)
1245 and counted before seeding ~200,000 cells in a 30 mm glass-bottom dish (Greiner
1246 Bio-One, Cat No 627860) containing the micropatterned grids in a small amount of
1247 DMEM. The cells were allowed to attach to the grids for 4-5 h before vitrification in
1248 liquid ethane using a Vitrobot Mark IV (ThermoFisher Scientific). The following
1249 settings were used; a chamber temperature of 37 °C, a chamber humidity of 85 %
1250 humidity, backside blotting with a 8.5 s blot time and blot force of -10 and a drain
1251 time of 1 s.

1252 Confocal microscopy

1253 RPE1 cell phenotypes were studied using a Zeiss LSM710 laser scanning confocal
1254 microscope (Carl Zeiss GmbH). The cells were grown in 30 mm glass bottom dishes
1255 with 4 compartments (Greiner Bio-One, Cat No 627870) and imaged at 37°C using a
1256 Zeiss 63× oil immersion objective (Plan-Apochromat, DIC, 1.4 NA). Lipi-Blue was
1257 excited with a diode laser at 405 nm and fluorescent emission was detected after
1258 passing a suitable emission filter (410-500 nm) using a Multi Alkali photomultiplier
1259 tube. The lysosomal stain was excited using an argon ion laser at 488 nm and
1260 emission was detected using an emission filter (499-541 nm). MCherry-p62 was
1261 detected using a 543 HeNe543 laser and an emission filter set to 579-696 nm using
1262 a GaAsP photomultiplier tube. Image analysis and quantification were done using Fiji
1263 (ImageJ, version 2.14.0) (Schindelin et al., 2012) and a self-written routine in
1264 CellProfiler (version 4.2.6) (Stirling et al., 2021). Measurements were exported as
1265 .csv files and analyzed in OriginPro 2023 (OriginLab Corporation, version
1266 10.0.0.154). Vitrified grids and thinned lamellae were studied using a Zeiss LSM800
1267 upright laser scanning confocal microscope with a cryostage (Linkam CMS196).
1268 Super resolution images were acquired using a Zeiss 100x air immersion objective
1269 (EC Epiplan NeoFluar, DIC, NA=0.75) and an AiryScan Detector. MCherry-p62 was

1270 detected using a 561nm diode. Image processing was done using Zen Blue (Carl
1271 Zeiss GmbH, version 3.3.89).

1272 Correlative light and electron microscopy

1273 Cryo-lamellae were made in a correlative manner using the in-chamber METEOR
1274 fluorescence microscope (Delmic, Cat No 2707-999-0014-2) equipped with a
1275 LMPLFLN 50×, NA = 0.5, WD = 10.6 mm objective lens in the Aquilos2 cryo-FIB-
1276 SEM system (ThermoFisher Scientific). In short; micropatterned grids with RPE1
1277 cells were loaded under cryogenic conditions taking special care to avoid
1278 contamination build-up from air humidity. Cells were located using the electron beam
1279 and the sample was placed at eucentric height using MAPS software (ThermoFisher
1280 Scientific, version 3.19). Cell phenotype was confirmed by imaging each cell in the
1281 METEOR fluorescence microscope. Each cell was imaged using the focused ion
1282 beam and the location of the final 150 nm lamella was marked in AutoTEM
1283 (ThermoFisher Scientific, version 2.4.1). The lamellae were generated using a step-
1284 wise process; the cell was thinned to 1 µm with a 0.5 nA milling current, then thinned
1285 to 600 nm with a 0.3 nA current, next to 300 nm with a 0.1 nA current and finally
1286 thinned to 200 nm with a 50 pA ion beam. The final polishing step in which the
1287 lamella was thinned to 120-180 nm took place with a 30 pA ion beam. The final
1288 lamella was once again imaged using the METEOR fluorescence microscope and
1289 these images were used to determine where tomograms would be recorded. The
1290 lamella were coated with a thin platinum layer; sputtered for 7 seconds at 7 mA, to
1291 prevent sample charging. For a more detailed protocol see Berkamp et al. Bio-
1292 Protocols 2023 (Berkamp et al., 2023). Next, the samples were transferred under
1293 cryo-conditions to a 200 kV Talos Arctica G2 transmission electron microscope
1294 (ThermoFisher Scientific), equipped with a Bioquantum GIF (Gatan, Inc) and a K3
1295 direct electron detector (Gatan, Inc). Tilt series were recorded on p62 positive areas
1296 of the lamellae, using SerialEM (version 4.2.0)(Mastronarde, 2005) as movies at
1297 24,000x magnification with a 1.7435 Å/pixel size in super resolution mode and a
1298 dose of approximately 2.2 e/Å^2/tilt, 10 frames per tilt, and a total dose per tilt series of
1299 approximately 130 e/Å^2. All tilt series were recorded from -54° to 54° with 3°
1300 increments starting at the pre-tilt of the lamella, using a dose-symmetric bidirectional
1301 acquisition scheme with weighted dose according to tilt angle and a nominal defocus
1302 of -7 µm. The raw data was motion corrected and CTF corrected using WARP
1303 (version 1.0.9) (Tegunov & Cramer, 2019) and the tilt series were reconstructed
1304 using Aretomo2 (SBGrid) (Morin et al., 2013; S. Zheng et al., 2022). To aid the cryo
1305 tomogram visualization, they were deconvolved, denoised and the missing wedge

compensated using IsoNet (Liu et al., 2021) and cryoCARE (Buchholz et al., 2019). To aid in segmentation a pre-trained U-Net model for non-denoised data in MemBrain-Seg (version 9b) (Lamm et al., 2022) was used and the processed tomograms were then loaded into Amira 3D (ThermoFisher Scientific, version 2022.2) for semi-manual segmentation. Tomograms were visualized using the IMOD software package (version 4.11.20) (Mastronarde & Held, 2017). To aid in targeting the EDX spectra, high dose, single tilt micrographs were recorded on p62 positive areas of the lamellae at 24,000x and a dose of approximately 40 $e^-/Å^2$/micrograph and 180 frames per tilt with each a dose of approximately 0.24 $e^-/Å^2$. Motion correction for these micrographs was done in Relion (SBGrid, version 4.0.1) (Kimanius et al., 2021)

Energy-dispersive X-ray (EDX) spectroscopy

The in situ EDX experiments were carried out on a probe-corrected 200 kV FEI Titan microscope (ThermoFisher Scientific) fitted with a Super-X G2 quadrant detector EDX system (Bruker) and a Simple Origin dual grid cryo transfer holder (Simple Origin, Inc). The microscope was operated under cryo-conditions in STEM mode with a 1.5 mrad convergence angle, a 1 nm probe size at a magnification of 55,000, resulting in a 2.9 nm pixel size. EDX spectra were recorded with a 50 µs dwell time and 50 frames resulting in a total dose of 500 $e/Å^2$, a camera length of 3.5m and a detector dead time of approximately 70%. EDX spectra processing was done in Velox (ThermoFisher Scientific, version 3.14). Atomic map representations were rendered with a 12 px pre-filter average and a 12 px post-filter average for the p62 structures and a 25 px pre-filter average and a 9 px post-filter average for the lipid droplet and lysosome control experiments. The spectra were generated by segmenting the p62 coat in the HAADF-STEM micrograph and segmenting the same number of pixels in the lipid droplet core and a random area of the cytosol. This same process was followed for the control experiments.

Acknowledgements

S.B. was supported by a fellowship from the Alexander von Humboldt Foundation. This work was supported by the European Research Council under Grant Agreement 101118656 (ERC Synergy project 4D-BioSTEM). The work was initially supported by the Boehringer Ingelheim Fonds Exploration grant. The authors would like to thank Andreas Brech and Sebastian Schultz from Oslo University Hospital, Oslo, Norway for providing the stable mCherry-p62 RPE1 cell line. LT acknowledges the support India Alliance DBT/Wellcome trust grant (IA/21/2/505925). The authors

gratefully acknowledge the electron microscopy access time and computing time granted by the biological EM facility of the Ernst-Ruska Centre at Forschungszentrum Jülich. In particular, we thank Julio Ortiz for the recording of the Volta phase plate p62 filament tomograms. The authors gratefully acknowledge the computing time granted by the JARA Vergabegremium and provided on the JARA Partition part of the supercomputer JURECA at Forschungszentrum Jülich (Thörnig, 2021).

Author Contributions

SB, SM, LJ and CS designed the project. SM, AK, LJ purified p62 filaments. SM and AK determined the cryo-EM structure of p62. LJ and AK reconstituted p62 filaments with binding partners and LC3b conjugated liposomes. AK, OK and JF performed single-particle fluorescence measurements and analysis. SB performed the live cell confocal imaging and data analysis. SB performed in situ CLEM followed by cryo-ET analysis. SB, PL and RDB performed the EDX measurements and analus. SB, LJ, AK and CS wrote the manuscript with input from the other authors.

Competing Interest Declaration

The authors declare no competing interests.

Data and code availability

The EMDB accession number for the p62 cryo-EM map is EMD-51816.